Hysteresis-Suppressed Reversible Oxygen-Redox Cathodes for Sodium-ion Batteries

Natalia Voronina,[a] Min-Young Shin,[a] Hee-Jae Kim,[a] Najma Yaqoob,[b] Olivier Guillon,[b] Seok Hyun Song,[c] Hyungsub Kim,[c] Hee-Dae Lim,[d] Hun-Gi Jung,[d] Younghak Kim,[e] Han-Koo Lee,[e] Kug-Seung Lee,[e] Koji Yazawa,[f] Kazuma Gotoh,[g] Payam Kaghazchi,[b,*] Seung-Taek Myung[a,*]

[a]*Hybrid Materials Research Center, Department of Nano Technology and Advanced Materials Engineering, Sejong Battery Institute, Sejong University, Seoul, 05006, South Korea*

[b]*Forschungszentrum Jülich GmbH, Institute of Energy and Climate Research, Materials Synthesis and Processing (IEK-1), Jülich, Germany*

[c]*Neutron Science Division, Korea Atomic Energy Research Institute (KAERI), 111 Daedeok-daero 989 Beon-Gil, Yuseong-gu, Daejeon, 34 057, South Korea*

[d]*Center for Energy Storage Research, Korea Institute of Science and Technology, Seoul, 02792, South Korea*

[e]*Pohang Accelerator Laboratory, 80 Jigokro-127-beongil, Nam-gu, Pohang, Gyeongbuk 37673, South Korea*

[f]*Jeol Resonance Inc.,3-1-2 Musashino, Akishima, Tokyo 196-8558, Japan*

[g]*Department of Chemistry, Faculty of Science, Okayama University ,3-1-1 Tsushima-naka, Kita-ku, Okayama City 700-8530, Japan*

E-mail: p.kaghazchi@fz-juelich.de (P. Kaghazchi)
E-mail: smyung@sejong.ac.kr (S. Myung)

Keywords: Layered; Cathode; Oxygen redox; Sodium; Battery.

Abstract

Oxygen-redox-based cathode materials for sodium-ion batteries (SIBs) have attracted considerable attention in recent years owing to their possibility of delivering additional capacity in the high-voltage region. However, they still suffer from not only fast capacity fading but also poor rate capability. Herein, we introduce P2-$Na_{0.75}[Li_{0.15}Ni_{0.15}Mn_{0.7}]O_2$, an oxygen-redox-based layered oxide cathode material for SIBs. The effect of Ni doping on the electrochemical performance was investigated by comparison with Ni-free P2-$Na_{0.67}[Li_{0.22}Mn_{0.78}]O_2$. The $Na_{0.75}[Li_{0.15}Ni_{0.15}Mn_{0.7}]O_2$ delivered a specific capacity of ~160 mAh g^{-1} in the voltage region of 1.5–4.6 V at 0.1C in Na cells. Combined experiments (galvanostatic cycling, neutron powder diffraction (NPD), X-ray absorption spectroscopy (XANES), X-ray photoelectron spectroscopy (XPS), and nuclear magnetic resonance (^{7}Li NMR)) and theoretical studies (density functional theory, DFT calculations) confirmed that Ni substitution not only increases the operating voltage and decreases voltage hysteresis but also improves the cycling stability by reducing Li migration from transition metal (TM) to Na layers. This research demonstrates the effect of Li and Ni co-doping in P2-type layered materials and suggests a new strategy of using Mn-rich cathode materials *via* oxygen redox with optimization of doping elements for SIBs.

1. Introduction

Lithium-ion batteries (LIBs) are considered one of the most efficient types of rechargeable batteries for mobile electronics and electric vehicles owing to their high energy density and reasonable cyclability. As increasingly more devices require LIBs as power sources, it is necessary to search for alternatives to replace expensive lithium resources and reduce the cost of batteries. Among several candidates[1–3], the use of sodium-ion batteries (SIBs) has been shown to be particularly promising because of the even and abundant distribution of sodium resources on the earth's surface. Because of the large ionic size of sodium (1.02 Å) relative to that of lithium (0.76 Å), sodium transition metal (TM) oxides are typically stabilized into a layer structure[4-6]. The chemistry of sodium is particularly good with manganese in the oxide matrix, for example, Na_xMnO_2[7]; hence, the combination of earth-abundant elements is anticipated to further enhance the price merit of SIBs, provided that the performance is compatible with that of high-energy-density Ni-rich cathode materials for LIBs. Notwithstanding, there is an intrinsic demerit of SIBs, namely, the low operation voltage stemming from the high standard electrode potential of sodium metal (Na^+/Na: −2.7 V vs. standard hydrogen electrode (SHE)) compared with that of lithium metal (Li^+/Li: −3.04 V vs. SHE). To resolve this issue and for SIBs to compete with LIBs, the inherent disadvantage should be overcome by increasing the capacity as high as possible to achieve high energy density at a similar level as that of Ni-rich cathode materials for LIBs.

The above-mentioned cathode materials are solely activated *via* a cationic redox process; hence, there is a capacity limit attributed to the TM elements. The role of participating anions in the electrochemical reaction to deliver additional capacity was thus investigated, for example, oxidation of O^{2-} to $(O_2)^{n-}$ and *vice versa* on reduction in oxide matrices for layered compounds. Earlier works have demonstrated the validity of oxygen-redox reactions on Li-rich cathodes such

as $Li[Li_xTM_{1-x}]O_2$ in Li cells[8–10]. Interestingly, such oxygen behavior is also applicable to not only Na-rich cathodes[11–13], which are an analogue of Li-rich materials, but also Na-deficient TM oxides [14–21]. The Na-rich compounds are mainly based on noble and expensive TMs, such as 4*d* (Ru) and 5*d* (Ir) metals [22–24]; however, Na-deficient materials (P2 and P3) are represented by abundant and low-cost 3*d* (Mn)[15,16]. There is a universal notation for oxygen redox: $Na_x[A_yTM_{1-y}]O_2$, where TM is Mn[14–20], Ru[21,25,26], or Ir[23,27,28], and A is monovalent Li[14,17, 18,29,30] or divalent Mg[20,31–33] or Zn[34,35]. In this case, oxygen-redox activity is usually triggered by the presence of the Na–O–A configuration that forms lone-pair electrons in the O *2p* orbital, which allows subsequent oxidation of O^{2-} toward $(O_2)^{n-}$ in the bulk of cathode materials on desodiation and *vice versa* on sodiation. Yabuuchi et al.[17] introduced the first work on Li substitution at the Mn site in P2-$Na_{5/6}[Li_{1/4}Mn^{3.89+}{}_{3/4}]O_2$, delivering a discharge capacity of approximately 180 mAh g^{-1} with suppressed phase transition through rearrangement of cations after extraction of oxygen on a long voltage plateau over 3.5 V. Later work by de la Llave et al.[18] demonstrated that the density of states (DOS) of P2-$Na_{0.6}[Li_{0.2}Mn^{4+}{}_{0.8}]O_2$ for oxygen lying close to the Fermi-energy level indicates that oxygen is a possible redox center. In addition, the Li in the TM layers played an important role in improving the structure stability compared with that of P2-$Na_{0.6}MnO_2$. Rong et al.[36] investigated P2-$Na_{0.72}[Li_{0.24}Mn^{4+}{}_{0.76}]O_2$, which delivered a high discharge capacity of approximately 270 mAh g^{-1}, with extraction of all the sodium from the host structure with a charge capacity of 210 mAh g^{-1}. This property was attributed to the structural stability that maintained the P2 phase, though few small O2 phase domains were formed at the nanoscale when deeply charged during electrochemical reaction enabled by Mn^{4+}/Mn^{3+} and $O^{2-}/(O_2)^{n-}$ redox pairs. The structural stability was further reinforced by the addition of Ti in the TM layers, as $^{23}Na/^{7}Li$ solid-state nuclear magnetic resonance revealed that migration of Li from TM to Na sites was restrained during

charge[37]. As a result, P2-$Na_{0.72}[Li_{0.24}Ti_{0.1}Mn_{0.66}]O_2$ was able to retain a capacity as high as 76.6% after 50 cycles. Zhao et al.[14] observed a similar effect in F-doped P2- $Na_{0.65}[Li_{0.22}Mn_{0.78}]O_2$, which impeded oxygen loss from the structure in the desodiated state. Density functional theory calculation provides further insight for understanding the behavior of oxygen in these compounds. According to the calculation on $Na_{1-x}[Li_{1/3}Mn^{4+}{}_{2/3}]O_2$ by Kim et al.[38], the O 2*p* electron is oxidized to compensate for the charge imbalance, and a vacancy was observed around the oxidized O 2*p* electron. This finding indicates a linear increase as oxidation of oxygen further progressed. The above-mentioned theoretical phenomena were experimentally confirmed in P2-$Na_{0.6}[Li_{0.2}Mn_{0.8}]O_2$ [39]. However, one of the demerits of these compounds is the low operation voltage on discharge, which results in low energy density. Bruce et al.[39] circumvented the low operation voltage using ribbon-superstructured P2-$Na_{0.6}[Li_{0.2}Mn_{0.8}]O_2$, which exhibited a voltage plateau at approximately 3.8 V on discharge that is solely attributed to oxygen redox. $Mn^{4+/3+}$ redox was available below the voltage to reach the first discharge capacity of ~120 mAh g^{-1}. The uniqueness of this property was associated with local ordering of lithium and TM in the TM layers, such that there was no loss of oxygen but identification of electron holes in lattice oxygen that induces oxygen redox; however, migration of Li from the TM to Na site was inevitable, which may not be favored for capacity retention for long-term cycling. Thus, it is important to prevent not only out-of-plane migration but also in-plane migration for improving oxygen redox reversibility and suppressing voltage hysteresis.

Important aspect for minimizing voltage hysteresis between charge and discharge related to oxygen redox is to maintain oxygen stacking sequence together with the absence of irreversible gliding of the oxygen layers, as it was observed in layered $P\bar{1}$-type $Na_2Mn_3O_7$ ($Na_{4/7}[\square_{1/7}Mn_{6/7}]O_2$ with $\square_{Mn}$ vacancies) material.[40,41] $Na_2Mn_3O_7$ crystalizes in the layered triclinic $P\bar{1}$ structure, with

half of the sodium ions occupying the distorted prism sites (P) and the other half occupying distorted octahedral sites (O). Huq et al. showed that Na^+ extraction from the octahedral site is an essentially zero-strain process, proceeding through a single-phase reaction.[41] The extraction of sodium ions from the prismatic site occurred through a two-phase reaction ($P\bar{1}$-$R3$) with the shrinkage/expansion process of the vacant MnO_6 octahedron and a larger volume change during charge/discharge. However, the overall stacking sequence of oxygen ions was barely changed during both steps of Na^+ extraction/insertion, which differs from the behavior in P2/P3 cathodes of which extraction/insertion of Na^+ lead to the formation of O–P phases with simultaneous decrease of the interlayer distance. In addition, increasing the covalency of TM-O bond affects positively on maintenance of reversibility of oxygen redox reaction and decrease voltage hysteresis between charge and discharge. For example, non-hysteretic behavior was observed in Li_2IrO_3 due to the strong orbital overlap of TM and O, which helps to maintain a highly reversible oxygen redox process.[42] To conclude, impactful strategies toward clear understanding of reversibility of oxygen redox process and the nature of oxidized species are still under debate. In this regard, improvement of the material parameters and performance and in-depth understanding of the reaction mechanism are still urgently needed to achieve high-voltage and high-capacity electrode materials for SIBs.

Returning to P2-type materials, in order to increase operation voltage and suppress voltage hysteresis, our group circumvented the low operation voltage of P2-$Na_x[Zn_yMn_{1-y}]O_2$ by substituting a half of Zn^{2+} with Ni^{2+}, resulting in a high average voltage of approximately 3.5 V on discharge[34]. P2-$Na_{0.67}[Ni_{0.33}Mn^{4+}_{0.67}]O_2$[43-47] and P2-$Na_{0.67}[Li_{0.22}Mn^{4+}_{0.78}]O_2$[14,17, 18,29,30,36,39] are the most studied sodium layered materials. The former compound has high operation voltage and lower voltage hysteresis, while the P2-O2 phase transformation with severe volume change is

inevitable on charge, which leads to poor cycling performance. The latter one exhibits high capacity over 180 mAh g^{-1}, however, the compound presents demerits such as low operation voltage, a large voltage hysteresis between charge and discharge, and fast capacity fading. Thus, to offset the above-mentioned disadvantages of each material, it would be interesting to generate a compound with 1:1 ration for Li:Ni doping, for which the composition is adjusted to be $Na_{0.75}[Li_{0.15}Ni_{0.15}Mn_{0.7}]O_2$ to compensate charge balance. In this regard, use of elements with high electronegativity would be effective to stabilize the TM layers: Li (0.98) and Ni (1.91), of which, provided that Ni is present as Ni^{2+} additional reversible redox of Ni^{2+}/Ni^{4+} is also expected to show high operation voltage. In addition, the existing covalency by the presence of Ni^{2+}(Ni^{4+} in charged state)-O bond may reinforce the Li-O bond, such that the movement of lithium oxygen shared by Ni-O-Li in TM layers would be suppressed, compared with the Mn-O-Li bond in P2-$Na_{0.67}[Li_{0.22}Mn_{0.78}]O_2$. From the above findings, it is anticipated that suppressed migration of Li element is possible to improve the integrity of TM layers in P2-$Na_{0.67}[Li_{0.22}Mn_{0.78}]O_2$, which can retain the capacity for long term with high operation voltage. Therefore, we rationally designed the chemical composition of two materials with tetravalent Mn: $Na_{0.67}[Li_{0.22}Mn^{3.99+}{}_{0.78}]O_2$ (referred to as LM) and $Na_{0.75}[Li_{0.15}Ni_{0.15}Mn^{4+}{}_{0.7}]O_2$ (referred to as LNM). Both materials are crystallized into the P2-type layered structure but differ in the arrangement of cations in the TM layers. Namely, for LM, there is a random distribution of cations in the TM layers; however, for LNM, honeycomb Li/Ni/Mn ordering is present in the TM layers. As designated, the LNM material demonstrates higher operating voltage with suppressed voltage hysteresis. The P2–P'2 phase reaction is associated with charge compensation of the LM electrode by Mn^{3+}/Mn^{4+} and $O^{2-}/(O_2)^{n-}$ redox pairs. However, the LNM material presents phase transitions between the P2 and OP4 phase, accompanied by Mn^{3+}/Mn^{4+} and $O^{2-}/(O_2)^{n-}$ pairs with an additional contribution by the

Ni^{2+}/Ni^{4+} redox pair that is responsible for the rise of the operation voltage, as confirmed by X-ray absorption spectroscopy (XAS). Through ^{7}Li nuclear magnetic resonance (NMR, 2D pj - magic-angle turning and phase-adjusted sideband separation (MATPASS) pulse sequence), neutron powder diffraction (NPD), and density functional theory (DFT) calculation, we reveal that Ni substitution has a positive effect on reducing Li migration from TM toward Na layers and is identified as a key point of improving the electrode performance of LNM compared with LM material.

2. Results and Discussion

Structure analysis of P2-type LM and LNM

The X-ray diffraction (XRD) patterns of synthesized $Na_{0.67}[Li_{0.22}Mn_{0.78}]O_2$ (LM) and $Na_{0.75}[Li_{0.15}Ni_{0.15}Mn_{0.7}]O_2$ (LNM) compounds were refined using the hexagonal $P6_3/mmc$ space group (**Figure S1a and b**). For the refinement, the chemical compositions of the LM and LNM compounds were analyzed using inductively coupled plasma–atomic emission spectroscopy (ICP-AES), and the results were similar to the theoretical values (**Table S1**). The observed and calculated XRD patterns coincided, indicating that the materials were crystallized into a single P2 phase (**Table S2**). For LM, all the Bragg peaks were indexed with the $P6_3/mmc$ space group. In contrast, the LNM pattern has an additional peak at approximately $2\theta = 22°$, which does not belong to the $P6_3/mmc$ space group. It resulted from the cationic ordering of Li/Ni/Mn in the TM layer and formation of the superstructure[39]. Neutron powder diffraction (NPD) patterns provided further insight into resolving the Li local environment and superlattice structure to confirm the cationic ordering present in TM layers of LM and LNM. The NPD data clearly reveal additional superlattice peaks for the LNM material. Thus, we refined the NPD data using both $P6_3/mmc$ and $P6_3$ space

groups. As shown in **Table S3**, better refinements were made with the *P6$_3$/mmc* space group for the LM (**Figure 1a**), while the result suited the *P6$_3$* space group better for the LNM material with cationic ordering in the TM layer (**Figure 1b**). Rietveld refinement of LNM revealed that $\sqrt{3}a \times \sqrt{3}a$-type superlattice ordering (Li/Ni/Mn) in the TM layer with AB-type stacking sequence was present and matched the data, as reported by Yabuuchi et al.[17]. **Figure 1c** shows the crystal structure of both materials viewed along the *ab*-axis direction. The in-plane views show that Li and Mn are randomly distributed in the TM layers for LM, whereas the LNM has honeycomb ordering (Li/Ni/Mn) in the TM layers. By substitution of Ni, the resulting *a*-axis parameter increased from *a*=2.889 Å for LM to *a*=2.9018 Å for LNM and *c*-axis parameter decreased from *c*=11.1618 Å for LM to *c*=11.1535 Å for LNM. The increased *a*-lattice parameter for LNM is attributed to the difference in the ionic radii among Li^+ (0.76 Å), Mn^{4+} (0.53 Å), and Ni^{2+} (0.69 Å) and the decreased *c*-lattice parameter is associated with an increase in sodium concentration in LNM. We observed the Mn and Ni K-edge X-ray absorption near edge structure (XANES) for the as-synthesized LM and LNM materials (**Figure 1d and e**). The Mn K-edge spectra for LM and LNM are close to that of the $Mn^{4+}O_2$ reference, proving that Mn is stabilized as Mn^{4+} (**Figure 1d**). The Ni K-edge spectra for LNM is identical to that for the $LiNi_{0.33}^{2+}Co_{0.33}Mn_{0.33}O_2$ reference (NCM 333), indicating that the average oxidation state of nickel is 2+ (**Figure 1e**). Transmission electron microscopy (TEM) analysis with selected-area electron diffraction (SAED) along the [001] zone axis confirmed that LNM adopted the hexagonal crystal structure (**Figure 1f-1**). The TEM and SEM elemental mapping images indicate that Na, Ni, Mn, and O elements were homogenously distributed in the micron-sized LNM particles (**Figure 1f-2**–**5** and **Figure S2**).

Electrochemical Performance of LM and LNM

We firstly screened electrochemical performance of P2-$Na_{0.67}MnO_2$ (NMO), LM, and LNM electrode in Na cells at a current of 26 mA g^{-1} (0.1C) in the voltage range of 1.5–4.6 V (**Figure S3**). Since Li and Li/Ni dopings improved the corresponding electrochemical performances, we hereafter discuss details of sodium storage process of LM and LNM electrodes. The LM electrode delivered a first charge/discharge capacity of 147/180 mAh g^{-1} (**Figure 2a**). The differential capacity (dQ/dV) curve of the LM electrode presents one broad oxidation peak at 4.3 V upon charge and two reduction peaks at 3.0 and 1.7 V upon discharge (**Figure S4a**). The average oxidation state of Mn is close to 4+ in the pristine LM powder, and it is difficult to oxidize it further in the operation range; therefore, the delivered charge capacity can be solely attributed to $O^{2-}/(O_2)^{n-}$ redox. On discharge, a reversible $O^{2-}/(O_2)^{n-}$ redox occurs, followed by a Mn^{4+}/Mn^{3+} redox reaction that is consistent with the dQ/dV curve (**Figure S4a**). In contrast, the LNM electrode delivered a first charge/discharge capacity of 157/160 mAh g^{-1} (**Figure 2b**). The first charge curve consists of a sloppy region in the voltage range of 3.0–4.2 V, which may be associated with a two-electron transfer by oxidation of Ni^{2+} to Ni^{4+} and a flat plateau above 4.2 V that may be related to oxidation of O^{2-} to $(O_2)^{n-}$. The dQ/dV curve also presents two oxidation peaks at 2.8–3.5 V and 4.1–4.6 V, which correspond to Ni^{2+}/Ni^{4+} and $O^{2-}/(O_2)^{n-}$ redox pairs, respectively (**Figure S4b**). Upon subsequent discharge, the voltage profile shows a reduction peak at ~4 V accompanied by a long slope in the voltage range 2.5–3.75 V, after which gradual decay of the voltage is observed to the end of discharge. Delivered discharge capacity (160 mAh g^{-1}) may be responsible for the multiple reduction processes endorsed by $(O_2)^{n-}$ to O^{2-}, Ni^{4+} to Ni^{2+}, and Mn^{4+} to Mn^{3+} (**Figure 2b**). It is apparent that the Ni substitution and reduction of the concentration of

Li in the TM layers reduced the discharge capacity; however, it is surprising that the average operating voltage increased to ~3.3 V for the LNM electrode (compared with ~2.4 V for the LM one). In general, P2-type cathode materials usually have an abnormal coulombic efficiency (CE) at the first cycle due to the deficient sodium content in the compounds; however, the LNM electrode exhibited a surprisingly high CE of 98% compared with that for the LM electrode (81%). The Ni substitution also definitely improved the cycling performance, showing 73% retention for 300 cycles (**Figure 2c**). Despite the higher initial capacity of the LM electrode, it underwent serious fade in capacity over prolonged cycles, with almost no capacity after 300 cycles. Such a difference would be the result of the repetitive redox reaction of Mn^{4+}/Mn^{3+} in the LM electrode, associated with Jahn–Teller distortion of MnO_6 octahedra in the structure. In addition, the calculated specific energy densities of the LM and LNM electrodes were 431.3 and 498.9 Wh kg^{-1} for LM and LNM, respectively, at the first discharge. The high energy density was maintained to 302.4 Wh kg^{-1} for the LNM electrode, whereas the resulting energy density was disappointing at 80.6 Wh kg^{-1} for the LM electrode after 300 cycles.

The effect of Ni substitution is further highlighted by the rate performance (**Figure 2d–f**). The LNM electrode had better capacity retention of 88%, 82%, 76%, 70%, 62%, and 50% compared with the data obtained at 0.1C. The recovered capacity at 0.1C after the rate test reached approximately 94% (151 mAh g^{-1}) of the initial value obtained at 0.1C. In contrast, the charge transfer in LM was inferior to that for the LNM electrode. One of the reasons for these differences would be related to conductivity of the materials, improved by the Ni substitution from ~5×10^{-7} S cm^{-1} for LM to ~1×10^{-5} S cm^{-1} for LNM. Similarly, Choi et al.[42] reported similar tendency that Ni-doping in P'2 $Na_{0.67}[Ni_{0.05}Mn_{0.95}]O_2$ was effective to have better conductivity compared to that of P'2 $Na_{0.67}MnO_2$. The galvanostatic intermittent titration technique (GITT) was used to show the

improvement of the Na diffusion coefficient (D_{Na^+}). The diffusion coefficient of the LNM electrode was in the range of 1 x 10^{-10} to 6 x 10^{-10} cm^2 s^{-1}, whereas that of LM was in the lower range of 2 x 10^{-11} to 4 x 10^{-10} cm^2 s^{-1}. This higher D_{Na^+} for the LNM electrode was also responsible for the improved rate performance.

Structural Evolution during First Charge/Discharge Process

The *operando* XRD (*o*-XRD) patterns show the structural evolution of LM and LNM during the first cycle (**Figure 3**). As observed in **Figure 3a and b**, LM and LNM underwent different phase transitions during the first cycle. For LM upon charge (oxidation), the $(002)_{P2}$ and $(004)_{P2}$ peaks slightly shifted to lower angles (2θ), whereas the $(100)_{P2}$ and $(102)_{P2}$ peaks shifted to higher angles (**Figure 3a**). As Na^+ ions were extracted from the lattice, the interlayer expansion occurred because of the enlarged repulsive force in the structure, leading to an increase in the *c*-axis parameter (**Figure 4a**). Because of the inactive character of Mn^{4+} to 4.6 V on charge, the only active element is oxygen, which can participate in the oxidation process to deliver capacity for charge compensation. The small decrease of ~0.7% in the *a*-axis parameter in the LM can be attributed to the oxidation of oxygen during charge (**Figure 4a**). Note that the full desodiation induced the broadening of XRD peaks with small intensity at 4.6 V, despite having the P2 phase as a major phase. According to earlier works by Yabuuchi et al.[17] and Rong et al.[36], such alternation in the structure was attributed to the formation of O2-type stacking faults in the deeply desodiated state. Sodiation (reduction) gradually recovered it to the original P2 phase and the Bragg peak positions as well at 2.5 V. Broadening of the $(102)_{P2}$ and $(103)_{P2}$ peaks was observed in the range of 2–1.5 V, and the $(002)_{P2}$ and $(004)_{P2}$ peaks shifted to higher angles while the $(100)_{P2}$ and $(102)_{P2}$

peaks shifted to lower angles due to expansion of the *ab*-plane (*a*-axis) in the structure by reduction of Mn^{4+} toward Mn^{3+}. The $(100)_{P2}$ peak started to split into two peaks, 35.7° and 36.4° (2θ) below 2 V, of which the former peak at 35.7° (2θ) can be assigned to the P'2 phase, which is a distorted P2 phase, as more sodium ions were inserted on discharge. This finding suggests the phase transition P2–P2–P'2 for the LM electrode. The corresponding *a* and *c*-axis variations are summarized in **Figure 4a**.

In contrast, the LNM electrode showed a different tendency of phase transition from the LM electrode during the first charge/discharge (**Figure 3b**). While charging the LNM electrode to 4.3 V, the $(002)_{P2}$ and $(004)_{P2}$ peaks monotonically shifted to lower angles, with the $(100)_{P2}$ and $(102)_{P2}$ peaks shifting to higher angles, indicating a topotactic process of Na^+ extraction proceeding *via* a single P2-phase reaction. However, as the operation voltage increased above 4.3 V, the $(002)_{P2}$, $(004)_{P2,}$ $(100)_{P2}$, and $(102)_{P2}$ peaks became broader and shifted to higher angle with the P2–OP4 phase transition. Further pursuing the desodiation led to the disappearance of all the P2 peaks and emergence of a new $(004)_{OP4}$ peak belonging to the *P*6*m*2 space group at the end of charge. The calculated *a*-axis parameter varied almost twice larger (~1.2%) than the observed value for the LM (~0.7%) within P2 phase during charge, which may be related to the oxidation of Ni^{2+} to Ni^{4+} (**Figure 4b**). Meanwhile, at a high voltage plateau within P2/OP4 phase transition and oxygen oxidation *a*-axis lattice variation was comparable to the variation in *a*-axis parameter for the LM material during charge. The P2–OP4 phase transition caused contraction of the *c*-axis from 5.57 to 5.33 Å, as shown in **Figure 4b**. During sodiation, the P2–OP4 phase transition was reversible; therefore, the OP4 phase gradually disappeared until 3.75 V, and the P2 phase emerged again from 3.7 V with a recovered original high intensity. Neither broadening of the XRD peaks nor peak splitting of the $(100)_{P2}$ peak at the end of discharge were observed for the LNM electrode,

as shown in **Figure 3b**. As evident from the *o*-XRD data, a reversible P2–OP4–P2 phase transition was observed for the LNM electrode. The incorporation of divalent Ni into the TM layers in $Na_{0.75}[Li_{0.15}Ni_{0.15}Mn_{0.7}]O_2$ ensured improved structural stability during de/sodiation compared with that of the LM electrode because the LNM material preserved the original P2 phase at the end of discharge. This improved structural stability of LNM may play a role in the improved capacity retention compared with that of LM in **Figure 2**. The corresponding lattice parameter variations and volume differences are summarized in **Figure 4a and b,** and the structural transformations are schematized with the average interslab distances in **Figure 4c**.

Charge Compensation Mechanism

The X-ray absorption spectroscopy (XAS) spectra of the Mn and Ni K-edge present the electronic structure and local environment changes of Mn and Ni for the fresh, half charged (4.3 V for LM and 4.0 V for LNM), fully charged (4.6 V), half discharged (2.5 V for LM and 3.4 V for LNM), and full discharged (1.5 V) states (**Figure 5**). Upon charging (half charged and full charged), the Mn K-edge XANES spectra of LM and LNM electrodes were close to that of the reference MnO_2 (Mn^{4+}), indicating that Mn^{4+} did not oxidized higher than Mn^{4+} in the voltage range (**Figure 5a and b**). For the half discharge electrodes (2.5 V), the Mn K-edge XANES spectra of the LM electrode did not show shift to lower photon energy, which means that Mn oxidation state is still close to 4+. However, on full discharge (1.5 V) the Mn K-edge XANES spectra shifted toward the reference Mn_2O_3 (Mn^{3+}) due to the reduction of Mn^{4+} toward Mn^{3+}, estimated to be 3.65+ according to the linear calibration of the spectra (**Figure 5a**). The extended X-ray absorption fine structure (EXAFS) shows a small difference in the Mn–O distance (**Figure 5c**), indicating that the charged LM electrode exhibited a slight decrease in the Mn–O distance compared with

that of the fresh state, although Mn^{4+} remained constant throughout desodiation (**Figure 5a**). On the half discharge (2.5 V), the Mn–O and Mn–Mn distances did not notably vary due to inactive character of Mn at that voltage range (**Figure 5c**). However, after discharge to 1.5 V, both the Mn–O and Mn–Mn distances increased due to partial reduction of Mn^{4+} toward Mn^{3+} (**Figure 5c**). These changes in the interatomic distances coincide with the *a*-axis variation in the *o*-XRD data shown in **Figure 4a**. In contrast, there was limited change of the Mn K-edge spectra for the LNM electrode during de/sodiation (**Figure 5b**). No change in the Mn K-edge spectra was evident on charge (half charged to 4.0 V and fully charged to 4.6 V). On discharge, the initial Mn^{4+} remained constant for the half discharged electrode to 3.4 V (Mn^{4+}) but slightly shifted after discharged to 1.5V ($Mn^{3.92+}$) (**Figure 5b**). It is not evident to see the Mn–O distance, however, the slight increase in the Mn–Me distance was noticed for the fully discharged LNM electrode (**Figure 5d**). This Mn–Me distance shift is most likely affected by the redox reaction of Ni, which occupies the octahedral sites together with Mn. The limited variations in the Mn–O bond length and the FT amplitude on discharge clearly indicate less variation in the local structure of Mn in the octahedral environment in the TM layers in LNM than in LM. This difference is related to the effect of the Jahn–Teller Mn^{3+} ion in the MnO_6 octahedral environment in TM layers that may be more dominant in the LM ($Mn^{3.65+}$) than in the LNM ($Mn^{3.92+}$) when fully sodiated.

In addition, the Ni redox reaction was highly reversible for the LNM electrode (**Figure 5e**). The Ni K-edge spectra show a significant shift toward higher photon energy on half charge (higher than that for the $LiNi^{3+}_{0.8}Mn_{0.1}Co_{0.1}O_2$ (NCM811) reference), however, no substantial shift was observed after charging to 4.6 V, suggesting that of oxidation of Ni^{2+} to Ni^{4+} occurring over the range lower than 4.0 V. As a result, decreases in the Ni–O and Ni–TM interatomic distances were observed as Ni^{2+} was oxidized to Ni^{4+} (**Figure 5f**). On discharge, the oxidized Ni^{4+} was reduced

to the original state of Ni^{2+} (**Figure 5e**); therefore, the Ni–O and Ni–TM bond lengths increased (**Figure 5f**), indicating the reversibility of the Ni^{2+}/Ni^{4+} redox reaction in the LNM electrode. These local environment changes correspond to *a*-axis parameter decrease/increase obtained from *o*-XRD patterns on charge/discharge (**Figure 4b**).

Combined with the data shown in **Figure 5**, it is not possible to explain the capacity obtained in both the LM and LNM electrodes because the Mn in both electrodes was inactive on charge, whereas the delivered charge capacities were 147 and 157 mAh g^{-1} for the LM and LNM electrodes, respectively. To determine the activity of oxygen for the LM and LNM electrodes, *ex-situ* O K-edge XANES and XPS measurements were performed for the fresh, first charged, and discharged states (**Figure 6**). In the O K-edge XANES spectrum, the pre-edge region can be divided into two peaks at 528.7 and 530.8 eV (**Figure 6a and b**). However, on charge, compared with the fresh state, the relative higher intensity at approximately 529.8 eV as the shoulder peak was observed for both materials. This change in the O K-edge spectra is due to the the oxidation of O^{2-} to $(O_2)^{n-}$. Upon discharge to 1.5 V, the shoulder at 529.8 eV was disappeared and the O K-edge spectra recovered to the original state. Therefore, we confirm the reversibility of the oxygen-redox reaction for both the LM and LNM electrodes.

Ex situ XPS analyses provided further insight on the oxygen activity that was measured at 20-nm depth, corresponding to the bulk part of the materials, from the surface observed in macro mode (400 × 400 μm^2) (**Figure 6c and d**). For the fresh LM electrode, the XPS spectrum was refined into two peaks at 529.8 and 531.5 eV, corresponding to a lattice oxygen (O^{2-}) peak and carbon-oxygen bond (C=O) peak, respectively (**Figure 6c**). On charging to 4.6 V, a new peak appeared at 530.6 eV, originating from the oxidation of the lattice oxygen (O^{2-}) bonded with Mn and Li to oxidized oxygen $(O_2)^{n-}$. In addition, the intensity of the C=O binding energy at 531.5 eV

decreased, and a new C–O binding energy was observed at 533.2 eV. In the subsequent discharge process, the peak at 530.6 eV $(O_2)^{n-}$ disappeared, revealing that the oxidized oxygen was reduced to O^{2-} in LM. Turning to the case of LNM, three peaks were present for the fresh electrode: the lattice oxygen (O^{2-}) peak at 529.8 eV, the C=O peak at 531.5 eV, and the C–O peak at 533.2 eV (**Figure 6d**). Upon charging to 4.6 V, the lattice oxygen peak at 529.8 eV decreased, whereas development of the oxidized oxygen $(O_2)^{n-}$ peak was observed at 530.6 eV because of oxidation of the lattice oxygen. On discharge, the oxidized oxygen peak at 530.6 eV was no longer observed, indicating reduction of the oxygen. We further confirmed the activity of oxygen at the 10th and 50th cycles for both electrodes (**Figure S5**). For both charged electrodes LM and LNM, the oxidized oxygen $(O_2)^{n-}$ peak at 530.6 eV emerged at the 10th cycle, showing similar relative intensities (**Figure S5a and b**). Even at the 50th cycle charge, the emergence of the oxidized-oxygen binding energy was evident for both electrodes, indicating the reversibility of the oxygen-redox activity in LM and LNM during prolonged cycling (**Figure S5c and d**). Summarizing the above XAS and XPS results, the capacity was shown to be delivered by not only TM redox, such as Mn and Ni, but also by oxygen redox for both electrodes.

Ex situ electron paramagnetic resonance (EPR) measurements were performed to highlight insights on the redox chemistries in LM and LNM materials. Both LM and LNM materials present a broad symmetric EPR signal, which is centered at g = 1.99 in the perpendicular mode (**Figure S6**), which is ascribed to antiferromagnetically coupled Mn^{4+}-O cluster. The less broadening of the LNM signal in comparison to the LM is associated with the ferromagnetic correlation between Ni^{2+} and Mn^{4+} ions.[49] Upon charging to 4.6V the LM material shows EPR spectra with significantly decreased intensity of Mn^{4+} peak (**Figure S7a**). It is related to oxidation of oxygen from O^{2-} to $(O_2)^{n-}$ to keep the charge neutrality, because Mn^{4+} is unlikely to be far oxidized in

octahedral environment in this voltage range. The intensity was decreased due to decrease of the coupling between Mn^{4+} and newly formed $(O_2)^{n-}$, as it was expected previously by Hu et al.[14,37,50,51] Turning to full discharge (1.5 V), LM material demonstrated a prominent intensity decrease, which is in line with the reduction of Mn^{4+} ($t^3_{2g}e^0_g$) toward Mn^{3+} ($t^3_{2g}e^1_g$), which is EPR-silent.[17,37,50] Hu et al. showed similar tendency in X-band EPR spectra for LM material.[51] The extra signal with a g_{eff} of ~2.007 appeared upon desodiation, manifesting the formation of $(O_2)^{n-}$ (n = 1, 2, 3). The signal at g=2.007 is compatible with both O_2^- and O_2^{3-}.[52] The weakness of this signal in the current work can be related to the partial condensation of two O_2^{3-} pairs, which leads to the EPR-silent varieties of O^{2-} and O_2^{2-} according to $O_2^{3-}+O_2^{3-}\rightarrow 2O^{2-}+O_2^{2-}$. Thus, the weak EPR signal of oxygen species can be associated either with the remaining O_2^{3-} species that survived the condensation, or to superoxo O^{2-} species formed during oxidation of peroxo O_2^{2-} species in our work.

Different tendency of EPR change is observed during charge/discharge in the LNM electrodes, compared to the LM materials (**Figure S7b**). Upon charging of LNM electrode up to 4.6V, Mn^{4+} signal decays to almost zero, which implies the oxidation of Ni^{2+} to Ni^{4+}. As it was previously reported Ni^{4+}–O–Mn^{4+} exhibits much larger antiferromagnetic interactions in comparison with Ni^{2+}–O–Mn^{4+}, which could totally quench the EPR signal of Mn^{4+}.[50,53,54] However, on discharge the spectra of EPR was observed with almost restored the intensity, indicating the reversible reduction of Ni^{4+} to Ni^{2+} that the feature was significantly different from the reduction of Mn^{4+} to Mn^{3+} quenching of Mn^{4+} signal in LM.[14,37,50-54] The O-O dimerization is expected to take place in cathode materials with a large portion of Li ions in TM sites.[55] The Li ion migration from TM sites

to Li or Na sites during charging can lead to the dimerization of O anions that have lost their bonds to migrated Li ions.

Li migration upon Na^+ Intercalation/Deintercalation

House and Bruce et al.[39] reported that the migration of Li from TM to Na sites is one of the possible reasons for capacity fade in the P2-$Na_{0.6}[Li_{0.2}Mn_{0.8}]O_2$ cathode. To identify the Li local environment upon de/sodiation, we employed ^{7}Li solid-state nuclear magnetic resonance (ssNMR) with pj - magic-angle turning and phase-adjusted sideband separation (MATPASS) pulse sequence (MATPASS) pulse sequence, neutron powder diffraction (NPD), and time-of-flight secondary-ion mass spectroscopy (ToF-SIMS) measurements. **Figure 7a and b** present the ^{7}Li ssNMR spectra of LM and LNM for fresh powders and electrodes charged to 4.6 V and discharged to 1.5 V. According to the literature on Li_2MnO_3, the ^{7}Li NMR spectrum can be divided into two main regions, representing different Li environments: 0–1100 ppm (Li in Na layers) and 1100–2400 ppm (Li in TM layers)[56]. The resonance at 0 ppm is attributed to the surface-deposited diamagnetic Li species, such as Li_2CO_3 or LiF, formed by passivation reaction with the electrolyte[57]. In our work, the shifts at 2110 and 1964 ppm indicates that Li element exists in the TM layers for the fresh state for LM material (**Figure 7a**). After charging the LM electrode to 4.6 V, the intensity of shift in the range of 1100–2400 ppm decreased and a new shift centered at 650 ppm appeared, implying that a large portion (44%) of Li ingredient migrated from the TM to the Na layers. The Li content in Na and TM layers was obtained by integration of ^{7}Li pj-MATPASS NMR spectra recorded at charged state and is expressed as a percentage of the total Li content in LM. At the end of discharge, the shifts at 1100–2400 ppm regained again their intensities and the shift at 650 ppm disappeared, indicating that all the Li was reinserted back into the TM layers. For the LNM

electrode (**Figure 7b**), the shifts at 1800 and 1715 ppm indicate that Li is present in only TM layer, however the positions of Li shifts are somewhat different from that in LM, which stems from the presence of NiO_6 octahedron. In octahedral environment Ni is known to have a lower spin (Ni^{2+}, S=1) than Mn (Mn^{4+}, S=3/2), yielding weaker hyperfine interactions, which causes appearance of shifts at lower frequencies (1800 and 1715 ppm) for LNM.[58] On charge, there was a noticeable displacement of shift in the range of 1100–2400 ppm, which is consistent with oxidation of Ni^{2+} toward Ni^{4+} (due to spin difference of Ni^{2+}, S=1 vs. Ni^{4+}, S=0). Moreover, the decline of the intensity of 1921 ppm shift together with the emergence of broad shift at 450 ppm implying that migration of Li from octahedrally coordinated TM layers to sodium layers also occurs in the LNM material. However, in comparison with LM the degree of migration of Li from TM layer to Na layer in LNM material was diminished (44% for LM vs. 24% for LNM). Sodiation of LMN material showed disappearance of the shift at 450 ppm, indicating that all Li reinserted back into the TM layers. In conclusion, ^{7}Li NMR data confirm the reversibility of Li migration from TM to Na layer in both LM and LNM, however, the displacement degree of Li element was reduced in LNM material. It is thought that the presence of higher covalency Ni-O bond is more likely associated with the reduced migration of Li element from TM to Na layers during cycling in LNM material rather than the total Li content in LM (Li0.22) and LNM (Li0.15).

To further explore the Li migration in LM and LNM materials, we performed Rietveld refinement of the NPD patterns at discharged states (**Figure 7c and d**). We were not able to refine the charged NPD patterns for both electrodes because of the poor NPD intensities originating from the low crystallinity of the desodiated phases. The influence of in-plane ordering in improving the electrochemical performance was reported by Bruce et al.[39], varying synthetic conditions. This affects operation voltage, reduced voltage hysteresis, long-term stability due to suppressing Li

migration from TM to Na layers. For the discharged LM material, the Li occupancy in the TM layer decreased from 0.22 to 0.19 compared with the fresh state (**Table S4a**). This finding suggests that Li migration is quite reversible in LM material, which is consistent with the NMR data for LM (**Figure 7a**). For LNM material Rietveld refinement of the NPD data in the fully discharged state indicates almost no Li present in the Na layers, of which the occupancy of Li is close to that of the fresh powders (**Table S3b and S4b**). Moreover, refinement of the NPD pattern of LNM after the first discharge using the hexagonal $P6_3$ space group confirms that in-plane $\sqrt{3}a \times \sqrt{3}a$ honeycomb superlattice ordering (Li/Ni/Mn) was maintained in the TM layers (**Figure 7d**). These data clarify that Li returned to the same position in the TM layers with the long-range ordering after the first charge/discharge. Altogether, the ^{7}Li NMR experiments and NPD data revealed that the migration of Li was suppressed in the LNM electrode during the de/sodiation. This suppression is most likely affected by the presence of Ni in the TM layers, which substantially preserves the in-plane ordering of the structure. The in-plane ordering related compounds are summaried in **Table S5**.

To further trace the effect of improved reversibility of oxygen redox and cycling stability of LNM over the LM electrode, we performed ToF-SIMS and ICP-AES experiments in fully charged and discharged states (**Figure S8 and Table S1**). For the fresh LM and LNM electrodes, we observed several representative fragments: $LiCO_2^+$ (m = 51.00) originated from Li_2CO_3, Na_2O^+ (m=61.97) and NaC_2^+ (m=46.98) fragments stemming from Na_2O and Na_2CO_3 compounds, and NaF^+ (m=41.98) fragment by NaF, which are the main components to constitute cathode–electrolyte interphase (CEI) layers. We highlight on the $LiCO_2^+$ fragment to correlate Li migration and formation of Li_2CO_3 on the surface of LM and LNM electrodes. Li_2CO_3 is present on the surface of materials after synthesis. Further, as the electrodes were charged to 4.6 V, the intensity

of this fragment was significantly increased for the LM electrode (**Figure S7a**) compared with that of the LNM electrode charged to 4.6 V (**Figure S7b**). This difference can be attributed to the Li extraction from the inner structure toward the surface, resulting in Li_2CO_3 on the surface of the LM electrode on charge. As observed from the ICP-AES data (**Table S1a**), the reduced Li content in the charged compound indicates partial migration of Li from the Na layers toward the surface, presumably *via* migration from TM to Na layers during the desodiation process. Thus, the relative intensity of the $LiCO_2^+$ fragment appeared rather stronger than that of the fresh LM compound. In contrast, the analyzed Li content was approximately 0.13 for the charged LNM electrode (**Table S1b**), which is slightly lower than that of the fresh state (0.15). Thus, the relative intensity of the $LiCO_2^+$ fragment emerged as being lower than that of the LM electrode (**Figure S7b**). On discharge, a decrease in the relative intensity was observed for the $LiCO_2^+$ (m = 51.00) fragment. The ICP-AES data indicate that the lowered Li content (0.22 → 0.15) on charge was partially restored on discharge (0.15 → 0.19) for the LM electrode. In addition, a slight variation was observed for the LNM electrode (0.13 → 0.14). Therefore, the ToF-SIMS and ICP-AES results indicate that the LM electrode undergoes more progressive migration of Li from the active material.

The above results demonstrate that migration of Li from the TM to Na layers was reduced for the LNM material, and the disorder in the host structure by forming vacancies is suppressed in the TM layers. In addition, the higher covalency of the Ni–O bond compared with that of the Mn–O bond is also considered to suppress the migration of Li to Na layers. Because the electronegativity of Ni (1.91) is higher than that of Li (0.98) and Mn (1.55)[59], the stabilization of the structure can be established by the presence of more covalent character of Ni with oxygen, which shares the

bond with Li in TM layers for the LNM material. This can simultaneously support the environment to sustain the in-plane ordering that suppresses the migration of Li from the TM to Na layers.

Density Functional Theory (DFT) calculation

Using density functional theory (DFT) calculation, we simulated the effect of Ni on the stability of Li ions in the lattice and redox mechanism of LM cathodes. The atomic structures of $Na_{0.67}[Li_{0.22}Mn_{0.78}]O_2$, $Na_{0.11}[Li_{0.22}Mn_{0.78}]O_2$, $Na_{0.75}[Li_{0.14}Ni_{0.17}Mn_{0.69}]O_2$, and $Na_{0.22}[Li_{0.14}Ni_{0.17}Mn_{0.69}]O_2$ (**Figure 8**) were determined by performing an extensive set of coulombic energy and DFT calculations (**Figure S9**). The computed lattice parameters indicate a very small decrease in the *a*-axis parameter (from 2.90 Å to 2.89 Å) and *c*-axis parameter (from 11.00 Å to 10.98 Å) for $Na_x[Li_{0.22}Mn_{0.78}]O_2$ when x=0.67 → 0.11 (**Table 1**). The former trend agrees with our *o*-XRD measurement and is most likely due to the extraction of Na^+ and weakening of Na–Na repulsive interaction along the *a*-axis direction. However, the computed decrease in the *c*-axis value is not consistent with experiment. The reasons behind this may be as follows. i) The desodiation-induced small change in the *c*-axis, which is observed in experiment and computed with DFT, might lie within the uncertainty of both methods. ii) The migration of Li ions from TM to Na sites followed by their segregation to the surface of the cathode can increase the *c*-axis value such that the computed *c*-axis value becomes larger with desodiation, in line with our experimental result. Process ii) will be discussed in detail later in this manuscript. For the Ni-doped system, namely $Na_x[Li_{0.14}Ni_{0.17}Mn_{0.69}]O_2$, our DFT calculation indicates that the *a*-axis parameter decreases from 2.93 to 2.87 Å and that the *c*-axis increases considerably from 10.97 to 11.27 Å when x=0.75 → 0.22. The decrease in the *a*-axis after desodiation is most likely due to both the extraction of Na^+ and the oxidation of Ni cations. To determine the reason behind the expansion

of the *c*-axis, we computed the O–TM–O intralayer (*d*1) and interlayer (*d*2) distances, which determine the *c*-axis value: $c = 2(d1+d2)$. We found a similar trend for both $Na_x[Li_{0.22}Mn_{0.78}]O_2$ and $Na_x[Li_{0.14}Ni_{0.17}Mn_{0.69}]O_2$ in that *d*1 decreases while *d*2 increases with desodiation. The large expansion of the *c*-axis in the latter system is clearly due to the increase in *d*2, which is because of weakening of the electrostatic attraction between the O–TM–O layers with the extraction of Na ions. The shrinkage of *d*1 in both systems is due to the oxidation of reactive ions (*i.e.*, Ni and/or O), which will be discussed later. Although the *d*2 value for desodiated $Na_x[Li_{0.11}Mn_{0.78}]O_2$ expands, we do not find an increase in *c*-axis because this increase in *d*2 is smaller than the decrease in *d*1. The reason for the smaller increase in *d*2 for the system without Ni is because of Li migration. Our DFT calculation indicates that Li ions occupy TM sites in the discharged $Na_{0.67}[Li_{0.22}Mn_{0.78}]O_2$ system; however, half of them migrate spontaneously into Na sites after charging (**Figure S9**), namely in the $Na_{0.11}[Li_{0.22}Mn_{0.78}]O_2$ system. The calculated *c*-axis for this system with partial Li ions in Na sites is, however, considerably shorter than that for $Na_{0.67}[Li_{0.22}Mn_{0.78}]O_2$ with all the Li ions in Mn sites. This result is not consistent with our XRD data showing the expansion of the *c*-axis with desodiation. However, after removing the Li ions from the Na sites ($Na_{0.11}[Li_{0.22}Mn_{0.78}]O_2 \rightarrow Na_{0.11}[Li_{0.11}Mn_{0.78}]O_2$) and optimizing the lattice parameters, we observed that the *c*-axis value expands (**Figure 8**) and becomes more comparable to the experiment. Therefore, we conclude that Li ions tend to leave the $Na_{0.11}[Li_{0.22}Mn_{0.78}]O_2$ lattice. With the migration and segregation of more Li ions, the *c*-axis value most likely becomes larger when $x=0.67 \rightarrow 0.11$. A similar result was not observed for the Ni-doped system, in which only 1/5 Li ions migrate spontaneously from TM to Na sites.

To better understand the reason behind this phenomenon, we characterized the redox mechanism by computing the number of unpaired electrons (N_{unp}) on elements, spin density

differences (SDD), and bond lengths. For $Na_{0.67}[Li_{0.22}Mn_{0.78}]O_2$ ($Na_{24}Li_8Mn_{28}O_{72}$), the computed average value of N_{unp} ($\overline{N_{unp}}$) on all Mn cations is 3.08, showing a charge state of 4+ (**Figure 9c**). Upon desodiation of x=0.67 → 0.11, the calculated $\overline{N_{unp}}$ for all Mn cations became 2.95, indicating that Mn still remains in the charge states of 4+, as clearly observed in the SDD plot (**Figure 8**). A clear increase in $\overline{N_{unp}}$ and larger SDD (more blue features) of oxygen anions indicate that they undergo oxidation. In the $Na_{0.75}[Li_{0.14}Ni_{0.17}Mn_{0.69}]O_2$ ($Na_{27}Li_5Ni_6Mn_{25}O_{72}$) system, the calculated value of $\overline{N_{unp}}$ for 24/25Mn and 1/25Mn are 3.10 and 3.81, respectively, indicating that almost all the Mn cations have a charge state of 4+ **(Figure 9d)**. The predicted charge states for 5/6Ni ($\overline{N_{unp}}$=1.75) and 1/6Ni ($\overline{N_{unp}}$=1.13) cations are 2+ and 3+, respectively. With the desodiation of x=0.75 → 0.22, Mn remains in the charge states of 4+ ($\overline{N_{unp}}$ = 3.01). The computed $\overline{N_{unp}}$ for Ni cations indicates that most of them experience oxidation with desodiation. $\overline{N_{unp}}$ for one of the Ni cations is 2.32 (**Figure 9e** and **Table 2**). After analyzing the Bader charges on all the Ni cations (**Table S6**), we observed that this Ni is even more oxidized than the others. Considering a possible spin transition on this Ni, the average oxidation state of Ni cations is computed to be 3.46+. We also find that oxygen anions undergo oxidation, *i.e.*, N_{unp} and SDD feature on some oxygen anions increase with desodiation (**Figure 8, 9a and b** and **Table 2**). Nevertheless, the number of oxidized oxygen anions and their magnitude of oxidation are clearly smaller in the Ni-doped system. The reason of Li migration for $Na_{0.11}[Li_{0.22}Mn_{0.78}]O_2$ can now be understood in terms of bond lengths (**Table S7**). We observed that due to the ionic size of Li, the averaged bond length of $\bar{l}_{Li\text{-}O}$ in the Mn site cannot be shorter than 2.06 Å, as the value of $\bar{l}_{Li\text{-}O}$ was computed to be 2.08, 2.06, 2.11, and 2.06 Å, respectively, for Li ions in the TM sites of $Na_{0.67}[Li_{0.22}Mn_{0.78}]O_2$, $Na_{0.11}[Li_{0.11}Mn_{0.78}]O_2$, $Na_{0.75}[Li_{0.14}Ni_{0.17}Mn_{0.69}]O_2$, and $Na_{0.22}[Li_{0.14}Ni_{0.17}Mn_{0.69}]O_2$. Because of the oxidation of O, $\bar{l}_{Mn\text{-}O}$=1.95 Å becomes shorter by 0.05 Å for $Na_x[Li_{0.22}Mn_{0.78}]O_2$ when x =

0.67→ 0.11. This limits the space for Li ions, forcing them to leave the TM sites. However, for the Ni-doped system, $\bar{l}_{\text{Ni-O}}$ decreases from 2.05 to 1.89 Å when $x = 0.75 \rightarrow 0.22$. This provides enough space for Li despite the contraction of $\bar{l}_{\text{Mn-O}}$ from 1.94 to 1.91 Å when $x = 0.75 \rightarrow 0.22$ in $Na_x[Li_{0.14}Ni_{0.17}Mn_{0.69}]O_2$.

The oxidation of oxygen can be related to a high covalency of Ni^{4+} that leads to substantially increased oxygen density near the Fermi level. Calculating magnetic moment is also a reasonable approach to find what ions and how much they are oxidized. Our calculated magnetic moment clearly indicates relatively a low oxygen redox reactivity in P2-$Na_{0.75}[Li_{0.15}Ni_{0.15}Mn_{0.7}]O_2$ relative to that in P2-$Na_{0.67}[Li_{0.22}Mn_{0.78}]O_2$ in the range of 1.5 – 4.6 V, which shows a different tendency to the work by Li et al.[16] that Li substitution suppressed the oxygen redox activity in P2-$Na_{0.66}[(Ni_{0.25}Mn_{0.75})_{0.9}Li_{0.1}]O_2$ in the range of 1.5 – 4.4 V. It is noted that in our work we studied the effect of Ni substitution on P2-$Na_{0.67}[Li_{0.22}Mn_{0.78}]O_2$ and found a new mechanism that Ni substitution suppresses migration of partial Li ions from TM to the Na layers followed by their migration to the surface and formation of TM vacancy occur.

Restrained oxygen loss during cycling

In oxygen-redox-based materials, the oxidation of O^{2-} often induces the oxygen loss from the lattice, accompanied by structural rearrangements and shortening of the high voltage plateau with decrease of the discharge voltage. Therefore, we employed o*perando* differential electrochemical mass spectrometry (*o*-DEMS) to directly investigate whether electrochemical oxidation of O^{2-} proceeds with or without lattice oxygen loss from the crystal structure in LM and LNM electrodes during the first cycle (**Figure S10**). Oxygen loss was negligible for both LM and LNM electrodes in Na cells in the voltage range of 1.5-4.6 V (**Figure S10a and b**), which is consistent with the

result observed for $Na_{0.78}[Li_{0.25}Mn_{0.75}]O_2$ reported by Bruce et al.[60] However, the behavior was different with the works of Hu et al.[14,51] where obvious O_2 evolution was clearly observed at the end of initial charging in $Na_{0.66}[Li_{0.22}Mn_{0.78}]O_2$. Such difference in DEMS results can be related to the difference in the distribution of Li in these materials and degree of Li migration from TM to Na layers. In the work of Hu et al.[51], Li locates not only in TM layers but also in Na layers according to ^{7}Li NMR data for the fresh LM material, of which they interpreted it due to existence of local defects. Moreover, almost Li migrated from TM to Na layers on charge. However, in the present work, Li is located solely in TM layers for both LM and LNM materials in pristine states, and only 44% and 24% of Li were mobile to Na layer, respectively, during charge. Therefore, we can conclude that the charge compensation process undergoes via Mn^{3+}/Mn^{4+}, Ni^{2+}/Ni^{4+}, and $O^{2-}/(O_2)^{n-}$ redox pairs for both LM and LNM in this work, rather than loss of oxygen from the oxide lattice.

Structural stability of LNM

Finally, we analyzed the structural stability of the LM and LNM electrodes after extensive cycling (300 cycles) (**Figure S11**). The XRD patterns confirm that both the LM and LNM electrodes maintained the original P2 phase. For the LNM electrode, no obvious changes in the peak positions and widths were observed. However, the LM electrode underwent serious disordering of the structure, showing notable broadening of the $(100)_{P2}$, $(102)_{P2}$, $(103)_{P2}$, $(104)_{P2}$ XRD peaks and their shift to lower angle. Such behavior is attributed to the higher degree of Li migration from TM to Na layers and incomplete recovery of the TM layers due to the tendency of producing thicker CEI layers as the development of the $LiCO_2^+$ (m = 51.00) fragment was perceived for the cycled LM electrode (**Figure S12a**). This tendency was less recognized for the

LNM electrode due to reducing of the Li migration by the presence of Ni, which provides more covalent character to share oxygen bonded with Li in the TM layers (**Figure S12b**). Such a thin CEI layer is beneficial to transfer the charge carriers, Na^+, properly throughout cycles over the long term; therefore, the resulting capacity retention was outstanding (as high as 73% for 300 cycles) for the LNM electrode. Compared with the fresh state, the cycled LM experienced significant change in the lattice parameters after repetitive de/sodiation (**Table S8**). The unit volume change of LM was approximately 3.6% higher than that for the LNM material. Moreover, for LM electrode appearance of P'2 phase after 1st discharge and disappearance of it after 300th discharge is laying in sodium concentration, which was significantly reduced after 300 cycles for LM material (delivered capacity ~ 30 mAh g^{-1}). Formation P'2 phase is highly dependent on the concentration of sodium in P2 Na-Mn-O compounds. P'2 structure is originated by slight elongation of *b*-axis in the hexagonal P2 structure when a large amount of Na^+ is inserted into the P2-type Mn-based layered compound.[51] The composition reached $Na_{0.8}[Li_{0.22}Mn_{0.78}]O_2$ after sodiation to 1.5 V, of which P2 structure cannot be preserved for the high concentration of sodium in Na layers, so that the structure transforms to P'2. The resulting sodium concentration gradually lowers as evident capacity fading is seen during cycling (**Figure 2c**). Thus, the corresponding XRD pattern showed only P2 phase after 300 cycles due to the low sodium concentration in the compound (**Figure S11)**. The low relative intensity and broadened feature of XRD data also imply that the repeated Na^+ extraction/insertion induced disordering of the structure for LM material. Additionally, HRTEM analysis with SAED patterns along the [001] zone axis for the LM and LNM materials confirmed the maintenance of the original P2 crystal structure for LNM, whereas the disordering was inevitable for the LM material because of higher degree of Li migration showing streaks in the SAED pattern (**Figure S13**). We also observed Mn K-edge XANES

spectrum after 300 cycles for the LNM electrode, indicating that negligible change was observed in the average oxidation state of Mn compared to the LNM electrode discharged to 1.5 V at the first cycle (**Figure S14**). It is evident that dissolution of Mn was greatly suppressed in LNM electrode after 300 cycles, compared to the extensively cycled LM sample in a Na cell (**Table S9**). This would be ascribed to the main redox species of Ni^{2+}/Ni^{4+} and $O^{2-}/(O_2)^{n-}$ for the LNM, namely, diminished participation of $Mn^{3+/4+}$ redox by the increased average oxidation state of Mn in the LNM (discharged state $Mn^{3.92+}$) in comparison to the LM (discharged state $Mn^{3.65+}$) electrode.

Based on our results, we can conclude that co-doping of Li and Ni into the TM layer positively affects the structural stability of Mn-rich oxygen redox-based P2-layered compounds. Li doping helps to activate the oxygen reaction and also prevents the P2–O2 phase transition, which usually occurs with significant structural changes. Ni, in turn, plays the role of a stabilizer of cationic ordering in the TM layer and suppresses Li migration to the Na alkali layer. As observed in **Figure 4**, it is obvious that compared with the lattice parameters of LM, the lattice parameters of LNM seem to change more during the charging and discharging process. It is known that the redox reaction of oxygen is slower and less reversible than that of TM. It is also known that Mn^{3+} ion exhibits Jahn-Teller distortion, which affects the cyclability of the material. Taking into the account the above facts, we can propose that LNM material showed better long-term cycling stability because the stable Ni^{2+}/Ni^{4+} redox is the dominant redox in this compound. In comparison, less stable $O^{2-}/(O_2)^{n-}$ and Mn^{3+}/Mn^{4+} redox are dominant in LM compound. The presence of higher covalency Ni-O bond affects reduced migration of Li element from TM to Na layers during cycling, promoting reversibility of oxygen redox reaction. Moreover, because of Ni doping, in addition to the average operation voltage and energy density increasing, the voltage hysteresis between charge and discharge curves is diminished and the capacity retention is greatly

improved. The schematic illustration of phase transitions, corresponding reaction mechanisms, and advantages for LM and LNM materials are presented in **Figure 10**.

3. Conclusions

In this work, we introduced P2-$Na_{0.75}[Li_{0.15}Ni_{0.15}Mn_{0.7}]O_2$ as an oxygen-redox-based cathode material. Through Ni substitution, we achieved stabilization of the Mn oxidation state at close to 4+ during prolonged cycling, decreasing the Jahn–Teller effect and resulting in better cycling performance and rate capability. *Operando* XRD revealed a reversible P2–OP4–P2 phase transition during cycling in the LNM electrode, with smaller structural change than that for the P2–O2 phase transition. The combination of experimental (NPD, ^{7}Li MAS ssNMR, and TOF-SIMS) and theoretical (DFT calculations) techniques revealed that migration of Li from the TM to Na layer, followed by its segregation as Li_2CO_3 on the cathode surface, was partially prevented by Ni doping. The charge-compensation mechanism was investigated using XANES, EXAFS, and XPS. Both cationic (Ni^{2+}/Ni^{4+} and Mn^{3+}/Mn^{4+}) and anionic ($O^{2-}/(O_2)^{n-}$) redox reactions were responsible for the delivered capacity. As a result, it has been shown that the presence of Ni in the TM layer of layered cathode materials is important for increasing the operation voltage, decreasing voltage hysteresis, suppressing Li migration, and improving cycling stability during prolonged cycling.

4. Experimental

See the Supplementary Information for details of the materials and methods.

Acknowledgements

N.V. and M.-Y. S. contributed equally to this work. The authors also greatly appreciate Prof. Shinichi Komaba (Tokyo University of Science, Japan) for fruitful discussion on this work. This work was supported by the Basic Science Research Program through the National Research Foundation of Korea (NRF), funded by the Ministry of Education, Science, and Technology of Korea (NRF-2017M3A7B4049173, NRF-2020R1A2B5B01095954, NRF-2020R1A6A1A03043435). P. K. gratefully acknowledges support from the "Bundesministerium für Bildung und Forschung" (BMBF) and the computing time granted through JARA-HPC on the supercomputer JURECA at Forschungszentrum Jülich.

Appendix A. Supplementary data

Supplementary data to this article can be found online at

References

[1] J. Y. Hwang, S. T. Myung, Y. K. Sun, *Chem. Soc. Rev,* **2017**, *46*, 3529.

[2] A. Konarov, N. Voronina, J. H. Jo, Z. Bakenov, Y. K. Sun, S. T. Myung, *ACS Energy Lett.* **2018**, *3*, 2620.

[3] J. Y. Hwang, S. T. Myung, Y. K. Sun, *Adv. Funct. Mater,* **2018**, *28*, 1802938.

[4] Y. Li, M. Chen, B. Liu, Y. Zhang, X. Liang, X. Xia, *Adv. Energy Mater.* **2020**, *10*, 1.

[5] Y. Zhang, X. Xia, B. Liu, S. Deng, D. Xie, Q. Liu, Y. Wang, J. Wu, X. Wang, J. Tu, *Adv. Energy Mater.* **2019**, *9*, 1.

[6] S. Shen, R. Zhou, Y. Li, B. Liu, G. Pan, Q. Liu, Q. Xiong, X. Wang, X. Xia, J. Tu, *Small Methods* **2019**, *3*, 1.

[7] A. Mendiboure, C. Delmas, P. Hagenmuller, *J. Solid State Chem*, **1985**, *57*, 323.

[8] A. D. Robertson, and P. G. Bruce, Chem. Mater, 2003, 15, 1984.

[9] A. R. Armstrong, M. Holzapfel, P. Novák, C. S. Johnson, S. H. Kang, M. M. Thackeray, and P. G. Bruce, *J. Am. Chem. Soc*, **2006**, *128*, 8694.

[10] K. Luo, M. R. Roberts, N. Guerrini, N. Tapia-Ruiz, R. Hao, F. Massel, D. M. Pickup, S. Ramos, Y. S. Liu, J. Guo, et al. *J. Am. Chem. Soc*, **2016**, *138*, 11211.

[11] N. Voronina, and S. -T. Myung, *Energy Mater. Adv*. **2021**, *2021*, 1.

[12] Y. Qiao, S. Guo, K. Zhu, P. Liu, X. Li, K. Jiang, C. J. Sun, M. Chen, H. Zhou, *Energy and Environ. Sci*, **2018**, *11*, 299.

[13] B. Mortemard De Boisse, G. Liu, J. Ma, S. I. Nishimura, S. C. Chung, H. Kiuchi, Y. Harada, J. Kikkawa, Y. Kobayashi, M. Okubo, A. Yamada, *Nat. Commu*, **2016**, *7*, 11397.

[14] C. Zhao, Q. Yang, F. Geng, C. Li, N. Zhang, J. Ma, W. Tong, B. Hu, *ACS Appl. Mater. Interfaces*, **2021**, *13*, 360.

[15] C. Zhao, Z. Yao, Q. Wang, H. Li, J. Wang, M. Liu, S. Ganapathy, Y. Lu, J. Cabana, B. Li, X. Bai, A. Aspuru-Guzik, M. Wagemaker, L. Chen, Y. S. Hu, *J. Am. Chem. Soc.* **2020**, *142*, 5742.

[16] B. Xiao, X. Liu, X. Chen, G. H. Lee, M. Song, X. Yang, F. Omenya, D. M. Reed, V. Sprenkle, Y. Ren, C. J. Sun, W. Yang, K. Amine, X. Li, G. Xu, X. Li, *Adv. Mater.* **2021**, *33*, 1.

[17] N. Yabuuchi, R. Hara, M. Kajiyama, K. Kubota, T. Ishigaki, A. Hoshikawa, S. Komaba, *Adv. Energy Mater*, **2014**, *4*, 1301453.

[18] E. de La Llave, E. Talaie, E. Levi, P. K. Nayak, M. Dixit, P. T. Rao, P. Hartmann, F. Chesneau, D. T. Major, M. Greenstein, D. Aurbach, L. F. Nazar, *Chem. Mater,* **2016**, *28*, 9064.

[19] T. Risthaus, D. Zhou, X. Cao, X. He, B. Qiu, J. Wang, L. Zhang, Z. Liu, E. Paillard, G. Schumacher, M. Winter, J. Li, *J. Power Sources*, **2018**, *395*, 16.

[20] R. J. Clément, J. Billaud, A. Robert Armstrong, G. Singh, T. Rojo, P. G. Bruce, C. P. Grey, *Energy and Environ. Sci*, **2016**, *9*, 3240.

[21] X. Cao, H. Li, Y. Qiao, X. Li, M. Jia, J. Cabana, H. Zhou, *Adv. Energy Mater*, **2020**, *10*, 1903785.

[22] N. Voronina, N. Yaqoob, H. J. Kim, K. S. Lee, H. D. Lim, H. G. Jung, O. Guillon, P. Kaghazchi, S. T. Myung, *Adv. Energy Mater,* **2021**, *11*, 2100901.

[23] A. J. Perez, D. Batuk, M. Saubanère, G. Rousse, D. Foix, E. McCalla, E. J. Berg, R. Dugas, K. H. W. van den Bos, M. L. Doublet, D. Gonbeau, A. M. Abakumov, G. van Tendeloo, J. M. Tarascon, *Chem. Mater,* **2016**, *28*, 8278.

[24] A. J. Perez, G. Rousse, J. M. Tarascon, *Inorganic Chemistry*, **2019**, *58*, 15644.

[25] M. H. N. Assadi, M. Okubo, A. Yamada, Y. Tateyama, *J. Mater. Chem. A,* **2018**, *6*, 3747.

[26] K. Jiang, X. Zhang, H. Li, X. Zhang, P. He, S. Guo, H. Zhou, *ACS Appl. Mater. Interfaces*, **2019**, *11*, 14848.

[27] X. Zhang, Y. Qiao, S. Guo, K. Jiang, S. Xu, H. Xu, P. Wang, P. He, H. Zhou, *Adv. Mater*, **2019**, *31*, 1807770.

[28] P. E. Pearce, G. Rousse, O. M. Karakulina, J. Hadermann, G. van Tendeloo, D. Foix, F. Fauth, A. M. Abakumov, J. M. Tarascon, *Chem. Mater,* **2018**, *30*, 3285.

[29] E. de La Llave, P. K. Nayak, E. Levi, T. R. Penki, S. Bublil, P. Hartmann, F. F. Chesneau, M. Greenstein, L. F. Nazar, D. Aurbach, *J. Mater. Chem. A*, **2017**, *5*, 5858.

[30] T. Jin, P. F. Wang, Q. C. Wang, K. Zhu, T. Deng, J. Zhang, W. Zhang, X. Q. Yang, L. Jiao, C. Wang, *Angew. Chemie - Int. Ed.* **2020**, *59*, 14511.

[31] N. Yabuuchi, R. Hara, K. Kubota, J. Paulsen, S. Kumakura, S. Komaba, *J. Mater. Chem. A*, **2014**, *2*, 16851.

[32] U. Maitra, R. A. House, J. W. Somerville, N. Tapia-Ruiz, J. G. Lozano, N. Guerrini, R. Hao, K. Luo, L. Jin, M. A. Pérez-Osorio, F. Massel, D. M. Pickup, S. Ramos, X. Lu, D. E. McNally, A. v. Chadwick, F. Giustino, T. Schmitt, L. C. Duda, M. R. Roberts, P. G. Bruce, *Nat. Chem*, **2018**, *10*, 288.

[33] H. J. Kim, A. Konarov, J. H. Jo, J. U. Choi, K. Ihm, H. K. Lee, J. Kim, S. T. Myung, *Adv. Energy Mater*, **2019**, *9*, 1901181.

[34] A. Konarov, H. J. Kim, J. H. Jo, N. Voronina, Y. Lee, Z. Bakenov, J. Kim, S. T. Myung, *Adv. Energy Mater*, **2020**, *10*, 2001111.

[35] W. Zheng, Q. Liu, Z. Wang, Z. Yi, Y. Li, L. Cao, K. Zhang, Z. Lu, *J. Power Sources*, **2019**, *439*, 227086.

[36] X. Rong, E. Hu, Y. Lu, F. Meng, C. Zhao, X. Wang, Q. Zhang, X. Yu, L. Gu, Y. S. Hu, H. Li, X. Huang, X. Q. Yang, C. Delmas, L. Chen, *Joule* **2019**, *3*, 503.

[37] C. Li, C. Zhao, B. Hu, W. Tong, M. Shen, B. Hu, *Chem. Mater*, **2020**, *32*, 1054.

[38] D. Kim, M. Cho, K. Cho, *Adv. Mater*, **2017**, *29*, 1701788.

[39] R. A. House, U. Maitra, M. A. Pérez-Osorio, J. G. Lozano, L. Jin, J. W. Somerville, L. C. Duda, A. Nag, A. Walters, K. J. Zhou, M. R. Roberts, P. G. Bruce, *Nature*, **2020**, *577*, 502.

[40] B. Mortemard de Boisse, S. ichi Nishimura, E. Watanabe, L. Lander, A. Tsuchimoto, J. Kikkawa, E. Kobayashi, D. Asakura, M. Okubo, A. Yamada, *Adv. Energy Mater.* **2018**, *8*, 2.

[41] B. Song, M. Tang, E. Hu, O. J. Borkiewicz, K. M. Wiaderek, Y. Zhang, N. D. Phillip, X. Liu, Z. Shadike, C. Li, L. Song, Y. Y. Hu, M. Chi, G. M. Veith, X. Q. Yang, J. Liu, J. Nanda, K. Page, A. Huq, *Chem. Mater.* **2019**, *31*, 3756.

[42] P. E. Pearce, A. J. Perez, G. Rousse, M. Saubanère, D. Batuk, D. Foix, E. McCalla, A. M. Abakumov, G. Van Tendeloo, M. L. Doublet, J. M. Tarascon, *Nat. Mater.* **2017**, *16*, 580.

[43] S. J. Park, J. Lee, I. H. Ko, S. Koo, S. H. Song, C. Koo, G. H. Yoon, T. Y. Jeon, H. Kim, D. Kim, S. H. Yu, *Energy Storage Mater.* **2021**, *42*, 97.

[44] A. Konarov, J. U. Choi, Z. Bakenov, S. T. Myung, *J. Mater. Chem. A* **2018**, *6*, 8558.

[45] Y. Zhang, M. Wu, J. Ma, G. Wei, Y. Ling, R. Zhang, Y. Huang, *ACS Cent. Sci.* **2020**, *6*, 232.

[46] K. Dai, J. Mao, Z. Zhuo, Y. Feng, W. Mao, G. Ai, F. Pan, Y. de Chuang, G. Liu, W. Yang, *Nano Energy* **2020**, *74*, 104831.

[47] A. Massaro, A. B. Muñoz-Garciá, P. P. Prosini, C. Gerbaldi, M. Pavone, *ACS Energy Lett.* **2021**, *6*, 2470.

[48] J. U. Choi, C. S. Yoon, Q. Zhang, P. Kaghazchi, Y. H. Jung, K. S. Lee, D. C. Ahn, Y. K. Sun, S. T. Myung, *J. Mater. Chem. A* **2019**, *7*, 202.

[49] M. Tang, A. Dalzini, X. Li, X. Feng, P. H. Chien, L. Song, Y. Y. Hu, *J. Phys. Chem. Lett.* **2017**, *8*, 4009.

[50] C. Zhao, C. Li, Q. Yang, Q. Qiu, W. Tong, S. Zheng, J. Ma, M. Shen, B. Hu, *Energy Storage Mater.* **2021**, *39*, 60.

[51] C. Zhao, C. Li, H. Liu, Q. Qiu, F. Geng, M. Shen, W. Tong, J. Li, B. Hu, *J. Am. Chem. Soc.* **2021**, *143*, 18652

[52] M. Sathiya, J. B. Leriche, E. Salager, D. Gourier, J. M. Tarascon, H. Vezin, *Nat. Commun.* **2015**, *6*, 1.

[53] H. Liu, C. Zhao, Q. Qiu, B. Hu, F. Geng, J. Li, W. Tong, B. Hu, C. Li, *J. Phys. Chem. Lett.* **2021**, 8740.

[54] J. Wang, M. Yang, C. Zhao, B. Hu, X. Lou, F. Geng, W. Tong, B. Hu, C. Li, *Phys. Chem. Chem. Phys.* **2019**, *21*, 24017.

[55] X. Li, Y. Qiao, S. Guo, Z. Xu, H. Zhu, X. Zhang, Y. Yuan, P. He, M. Ishida, H. Zhou, *Adv. Mater.* **2018**, *30*, 2.

[56] F. Dogan, J. R. Croy, M. Balasubramanian, M. D. Slater, H. Iddir, C. S. Johnson, J. T. Vaughey, B. Key, *J. Electrochemical. Soc*, **2015**, *162*, A235.

[57] O. Pecher, J. Carretero-Gonzalez, K. J. Griffith, C. P. Grey, *Chem. Mater*, **2017**, *29*, 213.

[58] K. Shimoda, K. Yazawa, T. Matsunaga, M. Murakami, K. Yamanaka, T. Ohta, E. Matsubara, Z. Ogumi, T. Abe, *Sci. Rep.* **2020**, *10*, 1.

[59] A. L. Allred, *J. Inorg. Nucl. Chem*, **1961,** *17*, 215.

[60] R. A. House, U. Maitra, L. Jin, J. G. Lozano, J. W. Somerville, N. H. Rees, A. J. Naylor, L. C. Duda, F. Massel, A. V. Chadwick, S. Ramos, D. M. Pickup, D. E. McNally, X. Lu, T. Schmitt, M. R. Roberts, P. G. Bruce, *Chem. Mater.* **2019**, *31*, 3293.

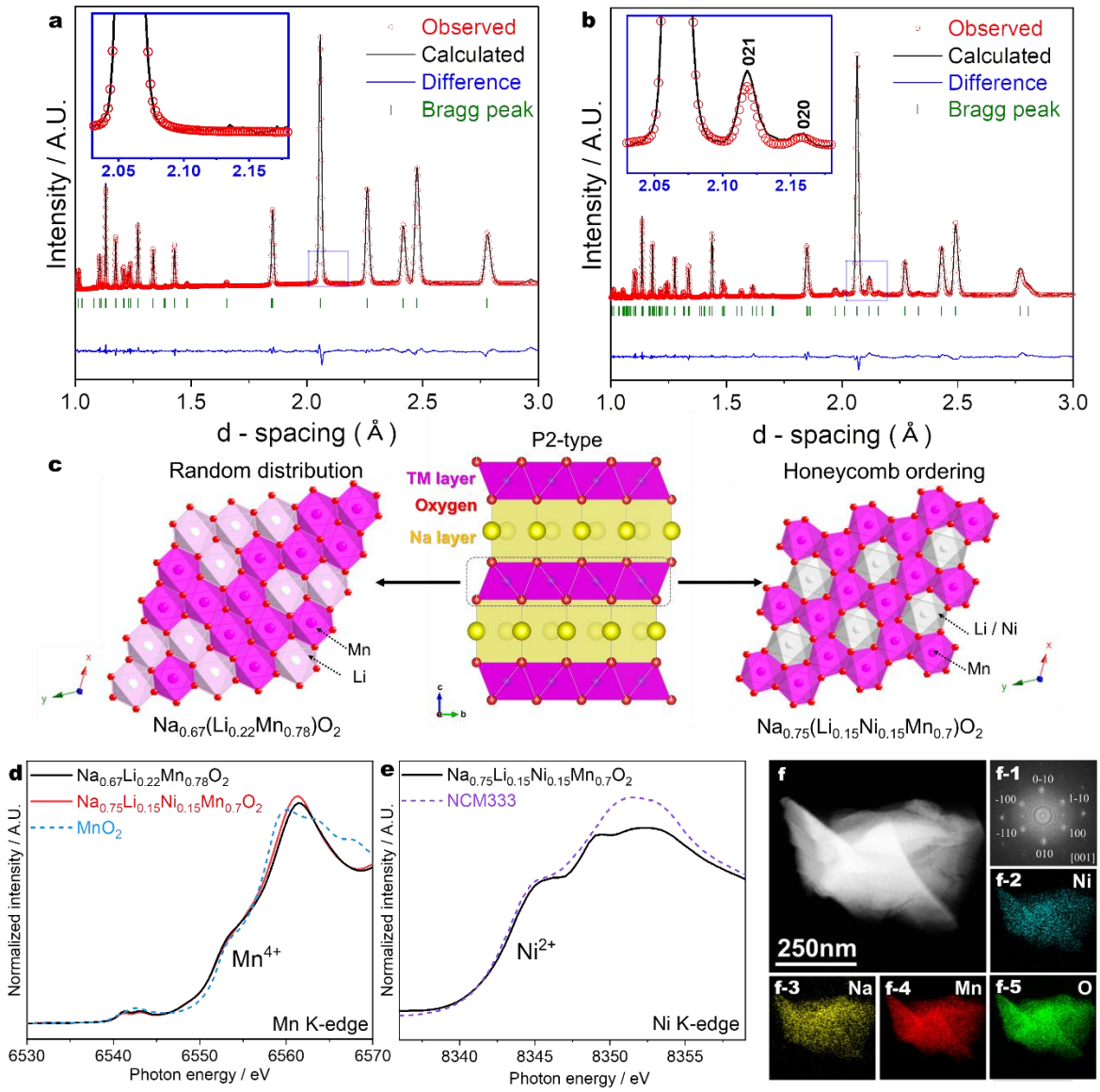

Figure 1. NPD patterns for as-synthesized (a) LM and (b) LNM compounds. Inset: expanded view of superlattice peak region; (c) Schematic illustration of crystal structure at different axis directions; XANES spectrum of (d) Mn K-edge and (e) Ni K-edge; (f) TEM images for LNM compound: (f-1) SAED pattern and (f-2~f-5) EDX mapping for Ni, Na, Mn, and O elements.

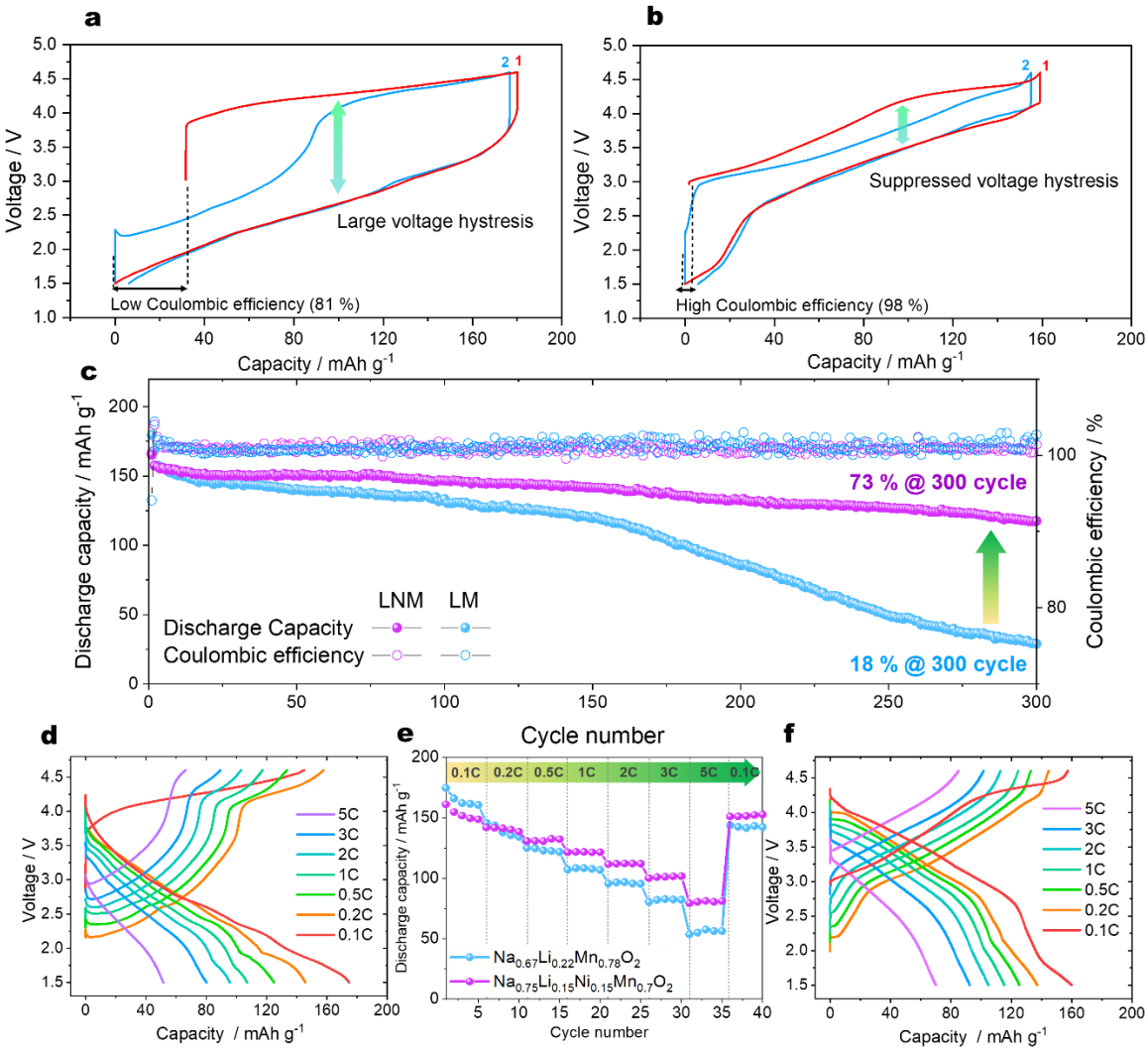

Figure 2. Electrochemical performance of LM and LNM electrodes. Voltage profiles of 1st and 2nd cycle (a) LM and (b) LNM electrodes tested at 0.1C; (c) Cycling performance at 0.1C for 300 cycles; Voltage profiles of (d) LM and (f) LNM compound at several C-rates (0.1 C – 5 C); (e) Rate performance for both electrodes at different current densities (0.1 C = 26 mA g-1).

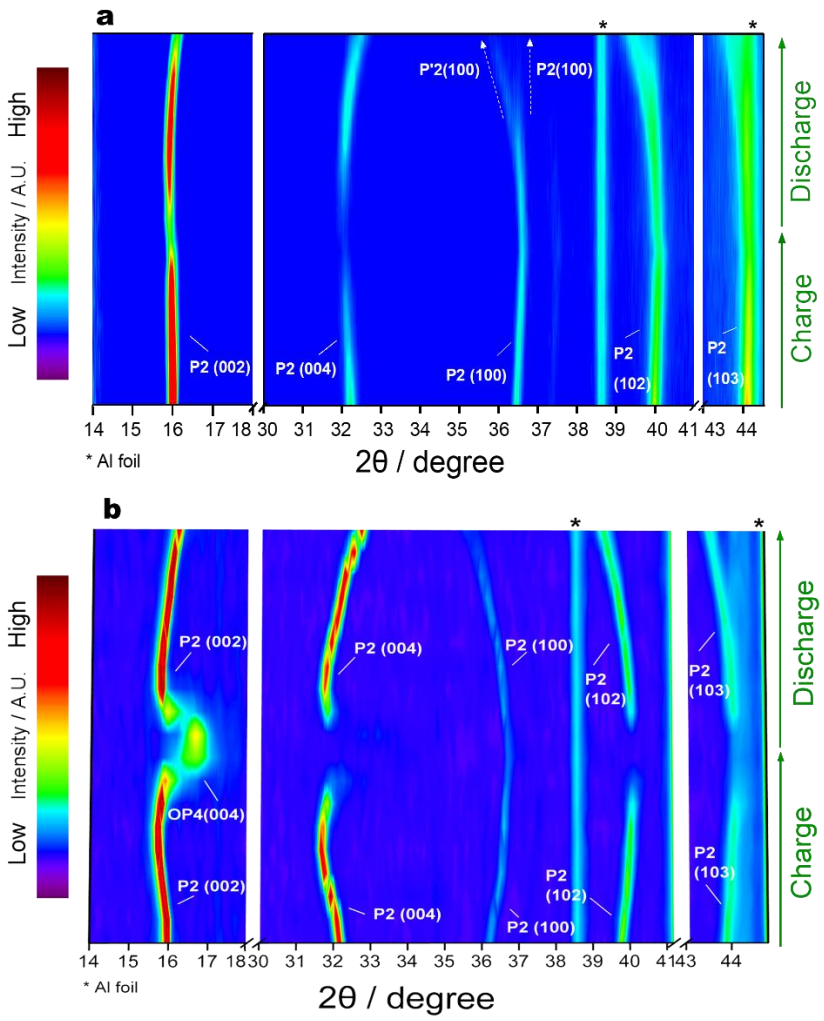

Figure 3. *Operando* XRD (*o*-XRD) patterns of (a) LM and (b) LNM electrodes measured with 0.1C during the first cycle. (*: Al current collector)

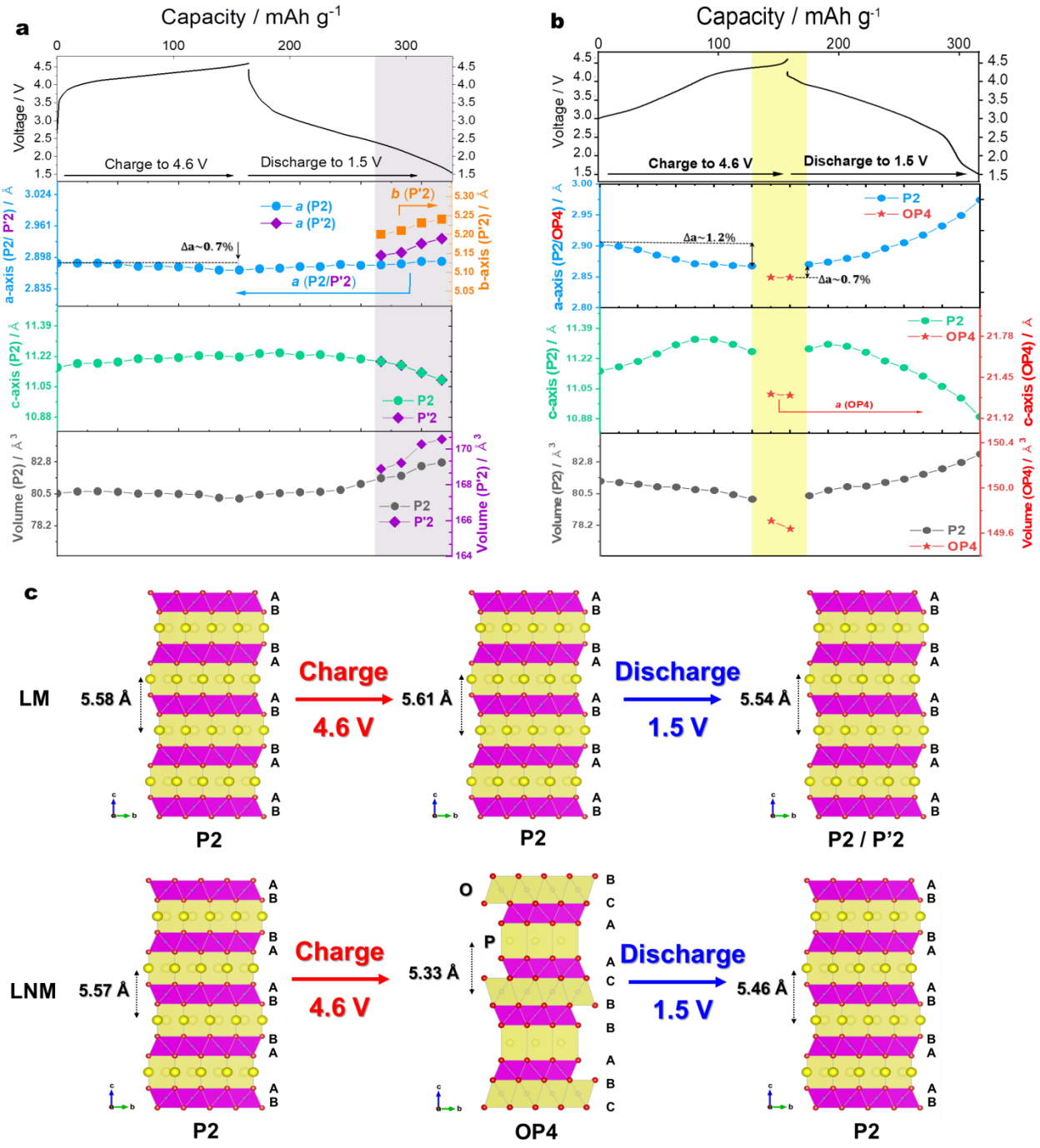

Figure 4. Lattice parameter variations for (a) LM and (b) LNM electrodes calculated from the *o*-XRD patterns; (c) schematic images of structural evolution during de/sodiation.

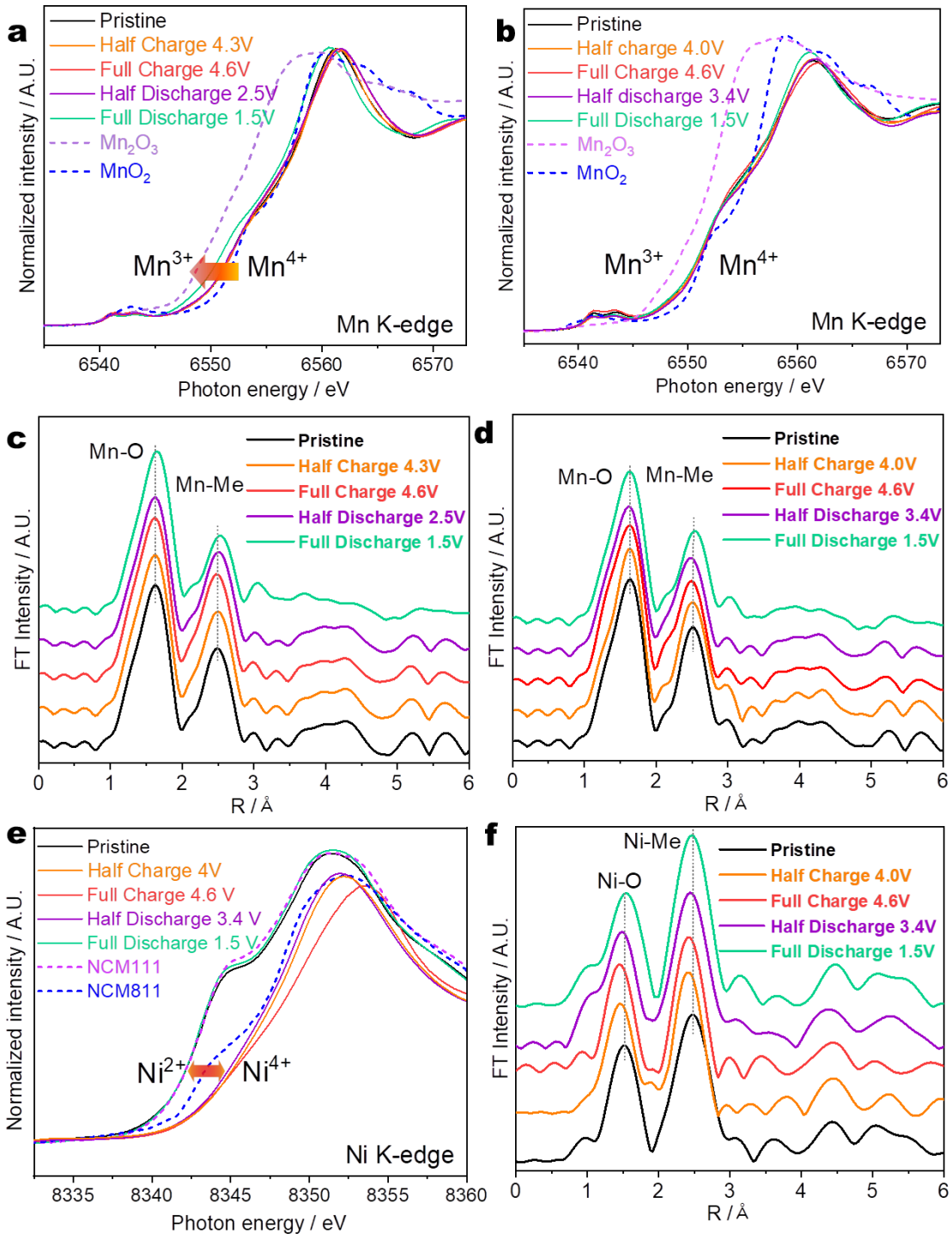

Figure

5. *Ex situ* XAS spectra for LM and LNM electrodes at different state: XANES spectra of Mn K-edge for (a) LM and (b) LNM; EXAFS spectra of Mn K-edge for (c) LM and (d) LNM electrodes; (e) Ni K-edge XANES spetra and (f) EXAFS spectra for LNM electrodes.

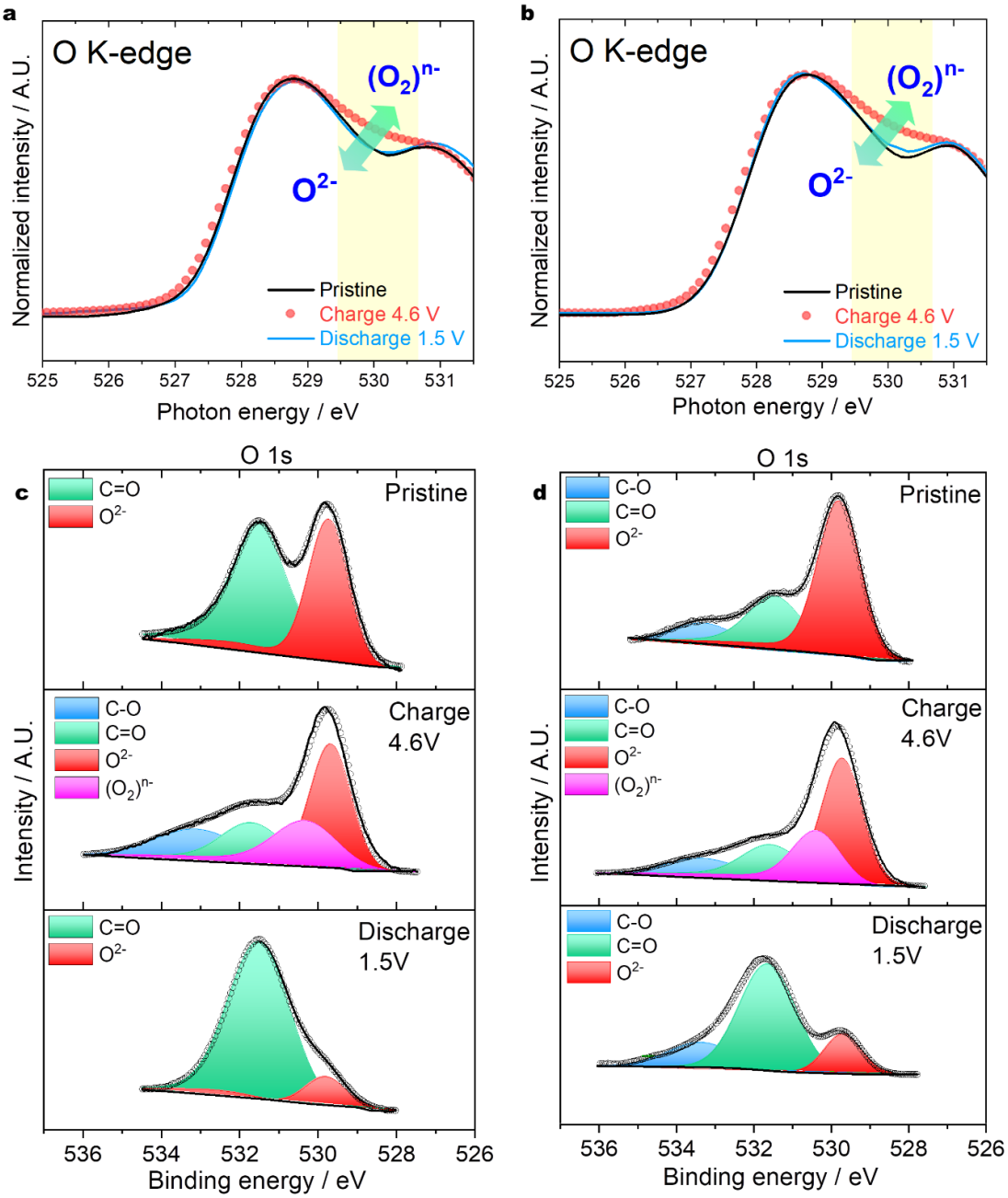

Figure 6. O K-edge XANES spectra of (a) LM and (b) LNM electrode, and XPS O 1s spectra of (c) LM and (d) LNM electrode at pristine, charge, and discharge states.

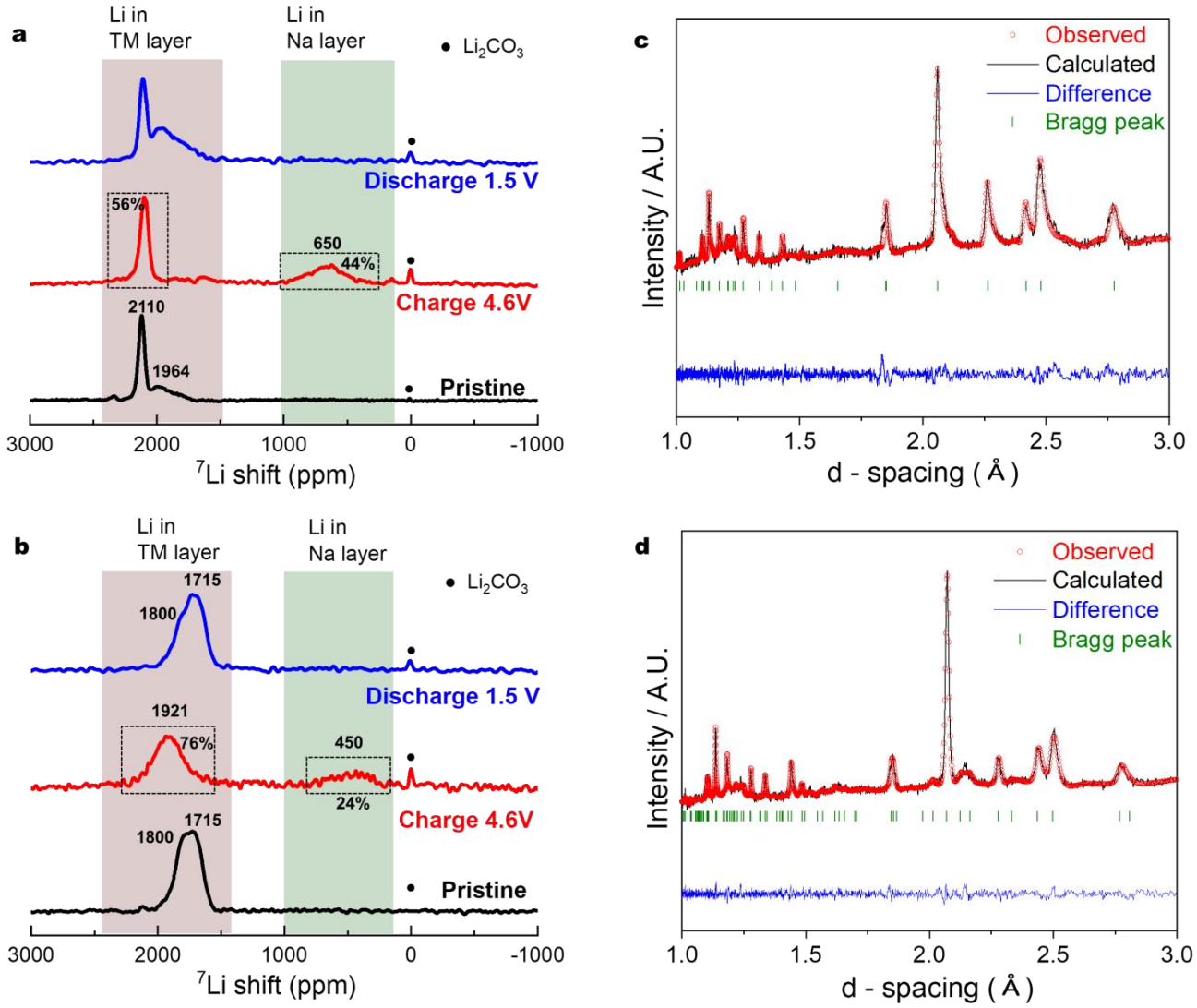

Figure 7. ^{7}Li MAS ssNMR spectra for (a) LM and (b) LNM materials. NPD patterns for (b) LM and (d) LNM electrode after first discharge to 1.5 V.

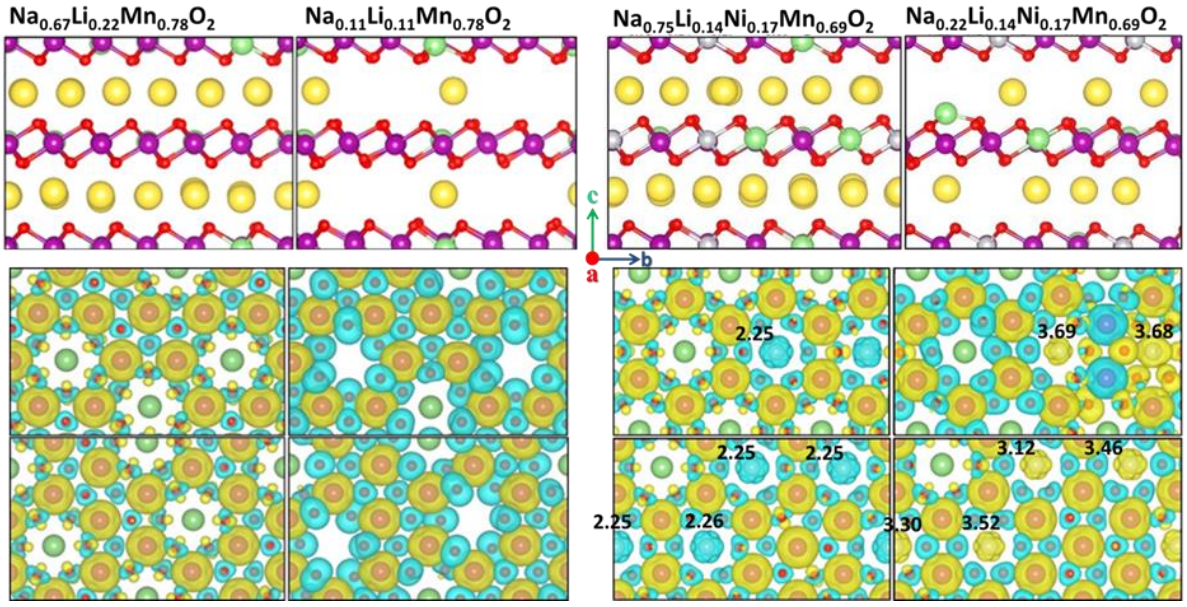

Figure 8. Calculated atomic structures (top) and spin density difference SDD plots (bottom) of LM and LNM before and after desodiation using DFT. Na, Li, Mn, Ni, and O are in yellow, green, purple, gray and red, respectively. An isosurface of 0.006 eV/Å^3 was used for the SDD plots. The up- and down-spin electrons are in yellow and blue, respectively. Charge states of Ni cations before and after desodiation are shown in the SDD plots.

System	*a*	*c*	*V*	*d1*	*d2*
$Na_{0.67}Li_{0.22}Mn_{0.78}O_2$	2.90	11.00	80.27	2.07	3.43
$Na_{0.11}Li_{0.11}Mn_{0.78}O_2$	2.89	10.98	78.50	2.00	3.49
$Na_{0.75}Li_{0.14}Ni_{0.17}Mn_{0.69}O_2$	2.93	10.97	81.05	2.09	3.40
$Na_{0.22}Li_{0.14}Ni_{0.17}Mn_{0.69}O_2$	2.87	11.27	80.42	1.99	3.64

Table 1. Calculated lattice parameters and volume as well as O−TM−O intralayer (d1) and interlayer (d2) distances using DFT: unit (a, c, d1 and d2: Å; volume: $Å^3$)

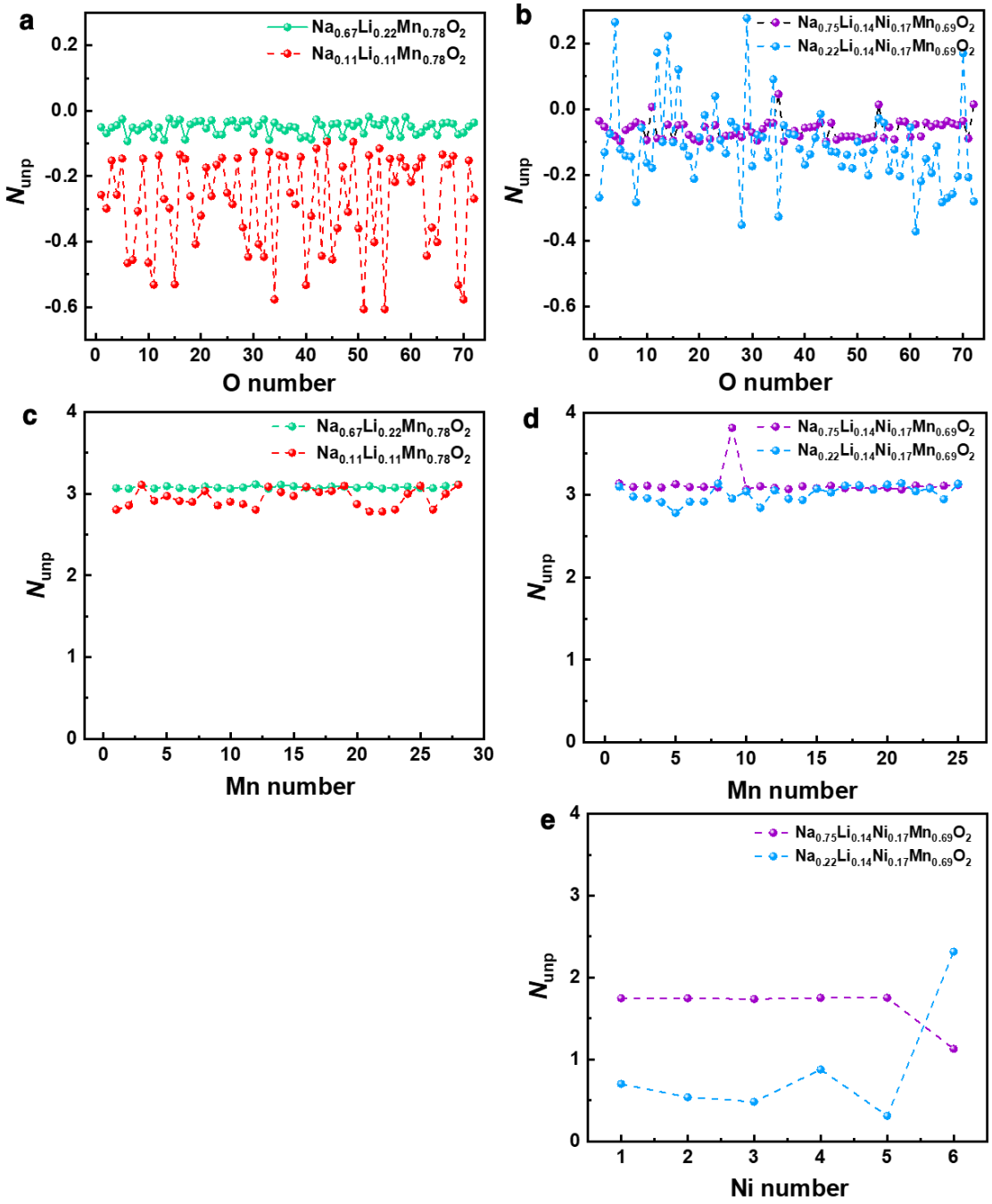

Figure 9. Calculated number of unpaired electrons N_{unp} on O anions for (a) LM and (b) LNM and on Mn for (c) LM and (d) LNM and on (e) Ni cations using DFT for $Na_{0.67}[Li_{0.22}Mn_{0.78}]O_2$, $Na_{0.11}[Li_{0.11}Mn_{0.78}]O_2$, $Na_{0.75}[Li_{0.14}Ni_{0.17}Mn_{0.69}]O_2$, and $Na_{0.22}[Li_{0.14}Ni_{0.17}Mn_{0.69}]O_2$.

System	Na	Li	Mn	Ni	O
$Na_{0.67}Li_{0.22}Mn_{0.78}O_2$	0.00	0.01	3.08	-	−0.05
$Na_{0.11}Li_{0.11}Mn_{0.78}O_2$	0.00	0.01	2.95	-	−0.28
$Na_{0.75}Li_{0.14}Ni_{0.17}Mn_{0.69}O_2$	0.00	0.01	$Mn_{24/25}$ = 3.10 $Mn_{1/25}$ = 3.81	$Ni_{5/6}$ = 1.75 $Ni_{1/6}$ = 1.13	−0.06
$Na_{0.22}Li_{0.14}Ni_{0.17}Mn_{0.69}O_2$	0.00	0.01	3.02	$Ni_{1/2}$ = 0.70 $Ni_{1/3}$ = 0.40 $Ni_{1/6}$ = 2.32	−0.11

Table 2. Calculated averaged number of unpaired electrons N_{unp} on cations and anions of studied cathode materials in their charged and discharged states using DFT.

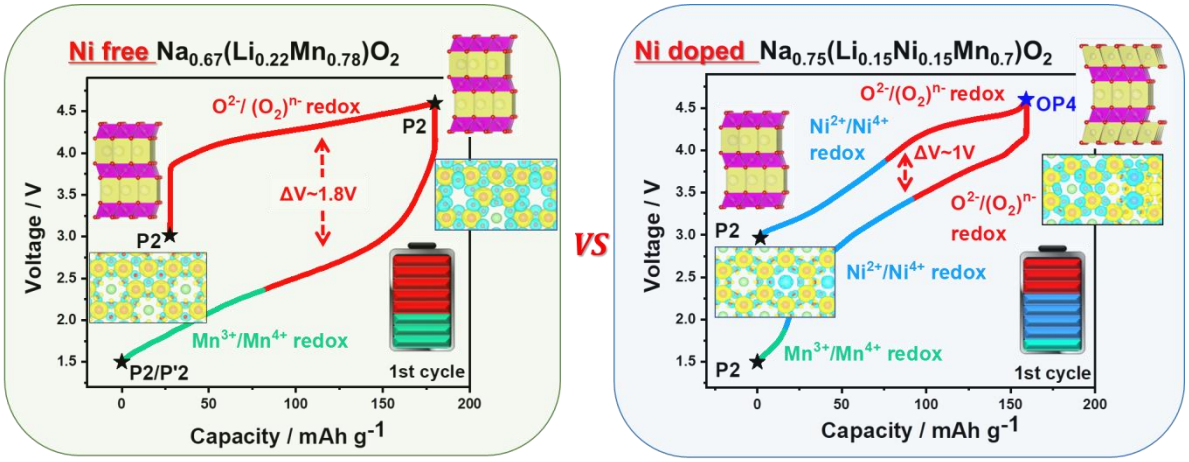

Figure 10. Schematic illustration of phase transitions and corresponding reaction mechanisms for LM and LNM.

We investigate the role of Ni substitution on the structure and electrochemical properties of oxygen-redox based P2-type $Na_{0.67}[Li_{0.22}Mn_{0.78}]O_2$ layered cathode material. Ni provides not only increase of the operating voltage and decrease of voltage hysteresis, but also improves the cycling stability by reducing Li migration from transition metal to Na layers.

Keywords: Layered; Cathode; Oxygen redox; Sodium; Battery.

Natalia Voronina, Min-Young Shin, Hee-Jae Kim, Najma Yaqoob, Olivier Guillon, Seok Hyun Song, Hyungsub Kim, Hee-Dae Lim, Hun-Gi Jung, Younghak Kim, Han-Koo Lee, Kug-Seung Lee, Koji Yazawa, Kazuma Gotoh, Payam Kaghazchi,* Seung-Taek Myung*

Hysteresis-Suppressed Reversible Oxygen-Redox Cathodes for Sodium-ion Batteries

TOC